

## TIDAL SYNCHRONIZATION OF TESS ECLIPSING BINARIES

MARSHALL HOBSON-RITZ <sup>1</sup>, JESSICA BIRKY <sup>1</sup>, LEAH PETERSON<sup>1</sup>, PETER GWARTNEY <sup>2</sup>, RACHEL WONG<sup>1</sup>,  
JOHN DELKER <sup>1</sup>, TYLER GORDON <sup>3</sup>, SAMANTHA GILBERT <sup>1</sup>, JAMES R. A. DAVENPORT <sup>1</sup> AND RORY BARNES <sup>1</sup>

<sup>1</sup>*Department of Astronomy, University of Washington, 3910 15th Avenue NE, Seattle, WA 98195, USA*

<sup>2</sup>*Department of Physics and Astronomy, University of Alabama, Tuscaloosa, AL 35487-0324, USA*

<sup>3</sup>*Department of Astronomy, University of California, Santa Cruz, 1156 High Street, Santa Cruz, CA 95064, USA*

### ABSTRACT

Tidal synchronization plays a fundamental role in the evolution of binary star systems. However, key details such as the timescale of synchronization, efficiency of tidal dissipation, final rotational period, and dependence on stellar mass are not well constrained. We present a catalog of rotation periods, orbital periods, and eccentricities from eclipsing binaries (EBs) that can be used to study the role of tides in the rotational evolution of low-mass dwarf (FGKM spectral type) binaries. This study presents the largest catalog of EB orbital and rotational periods ( $P_{\text{orb}}$  and  $P_{\text{rot}}$ ) measured from the *Transiting Exoplanet Satellite Survey* (*TESS*). We first classify 4584 light curves from the *TESS* Eclipsing Binary Catalog according to out-of-eclipse stellar variability type: starspot modulation, ellipsoidal variability, non-periodic variability, and “other” variability (e.g. pulsations). We then manually validate each light curve classification, resulting in a sample of 1039 candidates with 584 high-confidence EBs that exhibit detectable star-spot modulation. From there, we measure and compare the rotation period of each starspot-modulated EB using three methods: Lomb-Scargle periodograms, autocorrelation function, and phase dispersion minimization. We find that our period distributions are consistent with previous work that used a sample of 816 starspot EBs from *Kepler* to identify two populations: a synchronous population (with  $P_{\text{orb}} \approx P_{\text{rot}}$ ) and a subsynchronous population (with  $8P_{\text{orb}} \approx 7P_{\text{rot}}$ ). Using Bayesian model comparison, we find that a bimodal distribution is a significantly better fit than a unimodal distribution for *Kepler* and *TESS* samples, both individually or combined, confirming that the subsynchronous population is statistically significant.

### 1. INTRODUCTION

More than half of all stars are in binary star systems (Duquennoy & Mayor 1991; Raghavan et al. 2010; Duchêne & Kraus 2013), making them one of the most important objects in astrophysics. The orbits of binary stars enable direct constraints on fundamental stellar parameters, including masses and radii (Torres et al. 2018; Matson et al. 2016), as well as tidal interactions (Hut 1981; Meibom & Mathieu 2005; Meibom et al. 2006). In close systems, binary orbits evolve under the influence of tidal forces, as well as stellar evolution and magnetic braking (Witte & Savonije 2002; Repetto & Nelemans 2014; Penev et al. 2014; Bolmont & Mathis 2016; Song et al. 2018; Fleming et al. 2019; Zanazzi & Wu 2021). Similarly to single stars, each star loses rotational angular momentum due to magnetic braking amid magnetized stellar winds and mass loss (Skumanich 1972; Matt et al. 2015). Tidal forces drive an exchange of angular momentum between the orbital and rotational motions of the stars (Meibom et al. 2006). As

a result, tides dissipate orbital energy as heat, causing systems to evolve toward a state of dynamical equilibrium in which stellar rotation is coplanar and synchronized with the circular orbit (Counselman 1973; Hut 1980). The rate at which binaries approach tidal equilibrium strongly depends on the system’s orbital separation, eccentricity, obliquity, rotational speed, and stellar mass ratio (Hut 1981; Ferraz-Mello et al. 2008; Leconte et al. 2010). Therefore, constraining the process of tidal evolution in binary stars, particularly tidal synchronization, requires precise measurements of stellar rotation periods.

Prior to the era of time-domain surveys for measuring stellar variability (e.g., Borucki et al. 2010; Howell et al. 2014; Ricker et al. 2014; Chen et al. 2020; Jayasinghe et al. 2018), rotational velocities of stars were primarily obtained through spectroscopy, which measures the rotational broadening observed in spectroscopic absorption lines (Carroll & Ingram 1933; Gray 1976; Weise et al. 2010). However, constraints from spectroscopy are

limited to measuring only the rotational velocity times the projected line-of-sight angle ( $v \sin i$ ), which depends on the orbit inclination ( $i$ ) and stellar radius, which are difficult to constrain without further observations. Furthermore, spectroscopic rotational velocities require fitting or convolving a template atmospheric model to the spectra, making these constraints dependent on many modeling assumptions and complete line lists (Gustafsson et al. 2008).

In contrast to the spectroscopic method, light curve photometry allows for direct measurements of rotation periods from the quasiperiodic variation in starspots over time (Aigrain et al. 2012). Surveys including *Kepler* (Borucki et al. 2010), *K2* (Howell et al. 2014), and *Transiting Exoplanet Satellite Survey* (*TESS*; Ricker et al. 2014) have vastly expanded the number of stellar rotation measurements, allowing an understanding of how the dynamical evolution of a star depends on stellar properties (McQuillan et al. 2014; Gordon et al. 2021; Claytor et al. 2022; Angus et al. 2018, 2020). Furthermore, time domain surveys such as *Kepler* and *K2* have led to the discovery and characterization of thousands of eclipsing binaries (EBs; Prša et al. 2011; Kirk et al. 2016), including a number of discoveries in open clusters with varying ages (David et al. 2015, 2016; Gillen et al. 2017; Torres et al. 2018).

In one comprehensive study, Lurie et al. (2017, hereafter L17) used the *Kepler* eclipsing binary catalog (KEBC; Prša et al. 2011) to investigate the tidal synchronization rates of low-mass dwarf (FGKM spectral type) binary stars. The study aimed to contribute towards synchronization studies on late-type stars with convective envelopes (*e.g.* Giuricin et al. 1984; Claret & Cunha 1997; Meibom et al. 2006; Marilli et al. 2007). They measured rotation periods using star spot modulation to explore the effect of tidal synchronization on orbital period, eccentricity, mass ratio, and mass. All of these properties are important for tidal studies because they influence the rates of tidal interaction and evolution. The findings showed:

1. The majority of EBs at orbital periods less than 10 days are tidally synchronized.
2. There is a transition to higher eccentricity and pseudosynchronization (when eccentric binaries have a net torque of approximately zero, approaching torque equilibrium) at an orbital period of  $\sim 10$  days.
3. Synchronization has a stronger dependence on mass ratio when in the very small mass ratio regime.

4. In the FGK spectral type mass and radius range, there is no discernible dependence on primary star mass.

Alongside these important findings, an unexpected population of EBs was discovered that rotated typically 13% slower than synchronization. This population had low eccentricities, slightly favored lower mass ratios, and did not show any strong correlation with mass for the FGK primaries. Figure 1 compares the L17 results to the constant time lag simulations from Fleming et al. (2019), which assume a constant time lag interval ( $\tau$ ) of 0.1 seconds between the star’s tidal bulge and the passage of the tidally interacting companion. Subsynchronous binaries with spin-orbit frequency ratio  $\sim 7/8$  make up  $\sim 13\%$  of the L17 sample. Although the Fleming et al. (2019) models reproduced the 1:1 synchronized binaries and generated a wide distribution of subsynchronously rotating binaries, they fail to reproduce this tight overdensity at the 7:8 spin-orbit ratio. Fleming et al. (2019) found that variations in tidal parameters or initial conditions cannot recreate the L17 distribution. Furthermore, L17 found that the subsynchronous population is nearly circularized and shows no distinction from the rest of the sample in terms of primary star spectral type, leaving no obvious explanation for their existence.

There are several hypotheses for the origin of this overdensity of subsynchronicity. The L17 paper suggests that subsynchronicity is not mass dependent because no significant correlation was found between primary stellar mass and synchronization in the subpopulation and sample overall. Further evidence that mass is not relevant may be found in the stronger synchronization of the mass ratios in the small regime, which was marginally preferred in the subsynchronous sample. However, aside from mass dependence, there are still several remaining theories, such as period algorithm bias, instrumental bias, tidal forces, magnetic braking, stellar winds, and differential rotation.

In this work, we investigate two possible explanations for the subsynchronous population: the period-finding algorithm and instrumental bias. It is possible that the method used to measure the rotational period is an alias of a property of the light curve that produces the subsynchronous subsample. The L17 investigation was also limited by the faintness of *Kepler* targets ( $K_p < 17$ ; Vanderburg 2014) and the relatively small field of view (100 deg<sup>2</sup>). *TESS* is the ideal follow-up to these studies with approximately 85% sky coverage (2300 deg<sup>2</sup>), the ability to detect stars in numerous Galactic populations (including those in open clusters) (Fausnaugh et al. 2021). Note that the EB targets in the *TESS* field

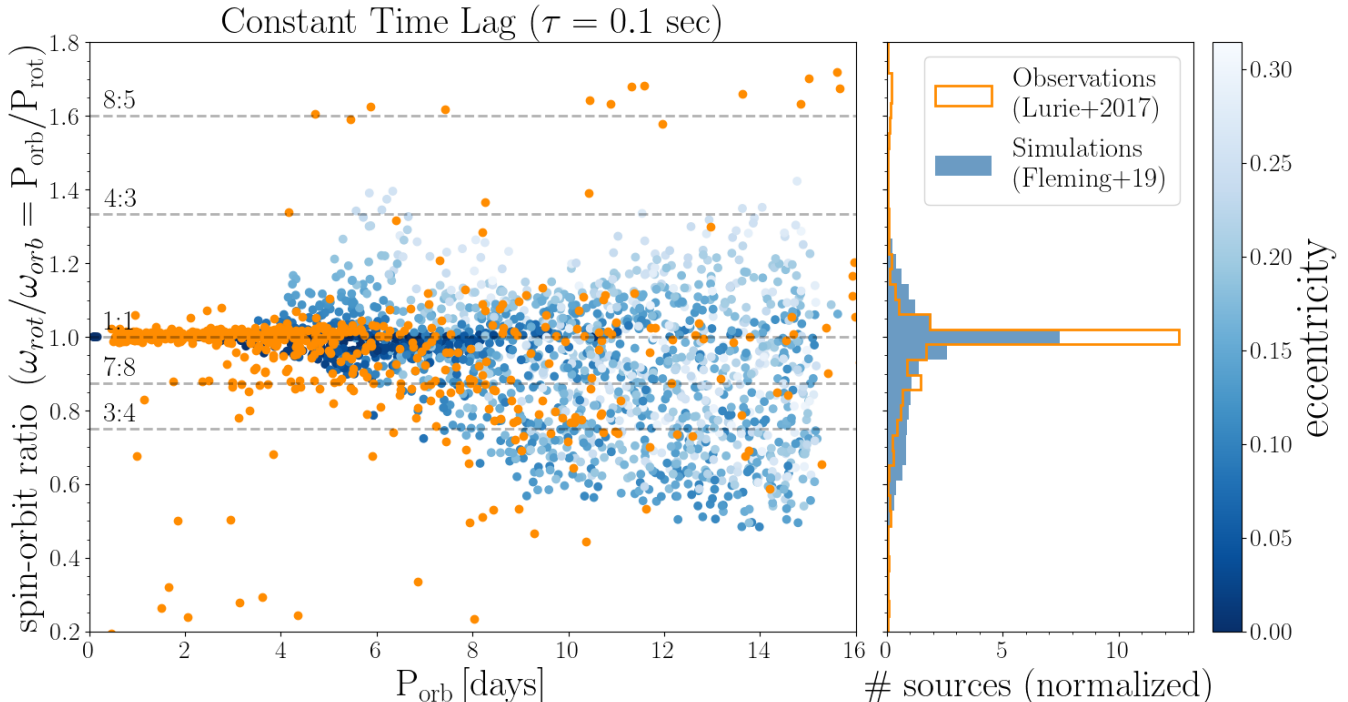


**Figure 1.** Distribution of spin-orbit ratios from observations compared to current constant-time-lag ( $\tau$ ) simulations. Orange points show binaries from *Kepler* (L17), and blue points show predictions from simulations (Fleming et al. 2019).

were selected according to eclipse detectability, rather than by apparent magnitude (Ricker et al. 2014).

We follow up on L17 to search for the subsynchronous population in a *TESS* EB sample. If the sub-population persists, it suggests that the phenomenon is not limited to only the observational field of *Kepler*.

Additionally, we look for period algorithm bias. We use the same Lomb-Scargle and autocorrelation period finding methods as in the L17 paper, but add the additional method of phase-dispersion minimization. We also visually inspect all rotational periods to confirm the automated results.

The remainder of the paper is organized as follows: Section 2 describes our data selection and classification process; Section 3 describes our procedure for measuring orbital and rotational periods; Section 4 compares the distribution of synchronized binaries to those presented in L17, and finally Section 5 discusses the implications of our results for constraining tidal synchronization as well as future work to be done in this area.

## 2. DATA

We start with the *TESS* EB catalog (hereafter TEBC; Prsa et al. 2021) which contains 4584 eclipsing binaries identified in the first two years (26 sectors) of the *TESS* survey (Ricker et al. 2014). The TEBC contains mea-

surements of the orbital period as well as a morphology parameter, which quantifies and effectively reduces the dimensionality of the light curve variability to a continuous variable in the range  $[0,1]$ , where a lower morphology value corresponds to more detached systems (Matijević et al. 2012).

We initially used the `lightkurve` package (Lightkurve Collaboration et al. 2018) with the SPOC pipeline to retrieve the first sector of data available for each target. For each target we download 2 minute cadence when available, otherwise we use the 30 minute cadence data. To better constrain the orbital periods of the longer period systems in our sample (6 to 10 days) we download all sectors of data available (each with  $\sim 28$  day lightcurves) to give at least 4 orbital periods worth of data. Later, we use all sectors of the data for each target once a subsample, as described in Section 4.

### 2.1. Variability Classification

Following L17, we classified each light curve into the following variability types: starspot modulations, ellipsoidal variations, other periodic variability, and nonperiodic. Figure 2 illustrates examples of the characteristic variability types found in *TESS* data.

1. **Starspot modulations (SP)** appear as quasiperiodic variations in the out-of-transit flux

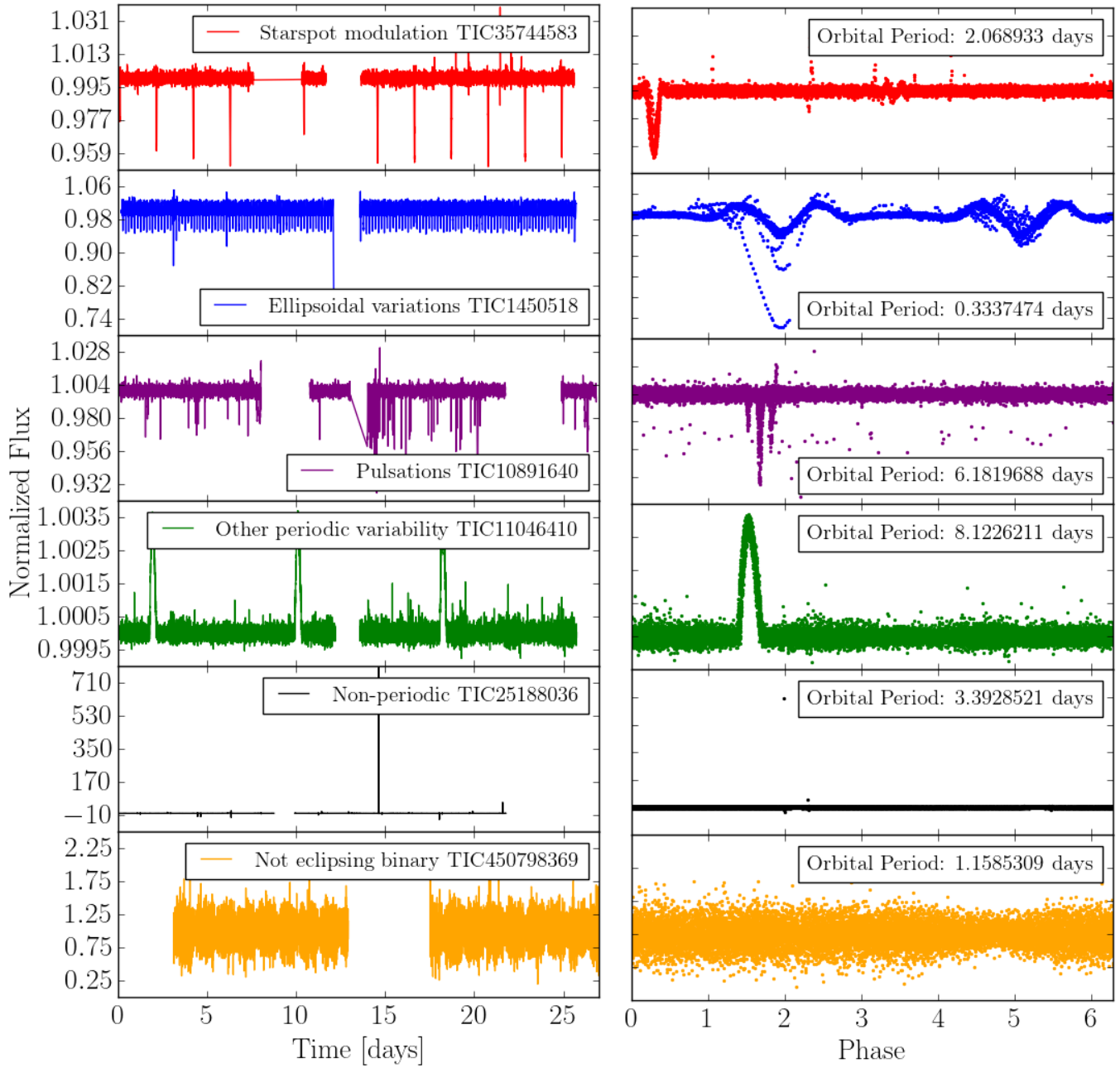


**Figure 2.** The left panel shows the light curve of an example of each classification type. The right panel shows the phase folded light curves for each classification type. These TICs are all from the TEBC.

due to dips in the brightness of the star as the spots rotate into and out of view. The shape of the variations changes over time as star spots form and evolve, as well as under the influence of differential rotation. Differential rotation is the phenomenon in which the rotation rate of a star decreases when moving from the equator to higher latitudes. For a star that exhibits differential rotation, star spots at different latitudes imprint different periodicities onto the star's light curve, resulting in interference patterns that change the shape of the variability over several periods (Lurie et al. 2017). When phase folded on the orbital period, the flux clearly shows the dips caused by the eclipses but has a shifting appearance of when the flux peaks in the orbit.

2. **Ellipsoidal variations (EV)** occur in very close binary systems and appear as two peaks in the light curve halfway between the primary and secondary eclipses. These variations result from the changing cross section in the orbit of tidally distorted stars as viewed from Earth. The largest cross section is at the quadrature, producing the observed pattern (Lurie et al. 2017). When phase folded on the orbital period, the flux shows a pattern with broadly winged dips from eclipses.
3. **Other periodic variability (OT)** are EBs that do not align to any of the described categories but still show periodic behavior. Some of these may be unidentified heartbeat stars or pulsations in one or both components (such as a  $\delta$  Scuti or  $\gamma$  Doradus companion). This category also includes non-eclipsing binaries, which are targets that are likely misclassified as EBs (such as fast rotators).
4. **Non-periodics (NP)** are EBs that do not exhibit clear out-of-eclipse variability. Many of these have essentially flat light curves, or variations dominated by noise.

### 3. METHODS

#### 3.1. Classification Procedure

Since we focus on systems with strong tidal interactions, we filter our sample to targets with orbital periods of  $P_{\text{orb}} < 10$  d. The dynamical evolution of these short-period systems is strongly impacted by tidal dissi-

pation. These are ideal for *TESS* observations, as they complete at least two orbits within a single *TESS* sector, which spans  $\sim 28$  days. Applying this selection left 3684 *TESS* light curves to classify. Next, we cross-match our filtered sample to the *Gaia* DR3 catalog to obtain the distances, as well as BP, RP, and G magnitude bands to use as features for the classifier (see Table 1).

**Table 1.** Features used in Random Forest classification.

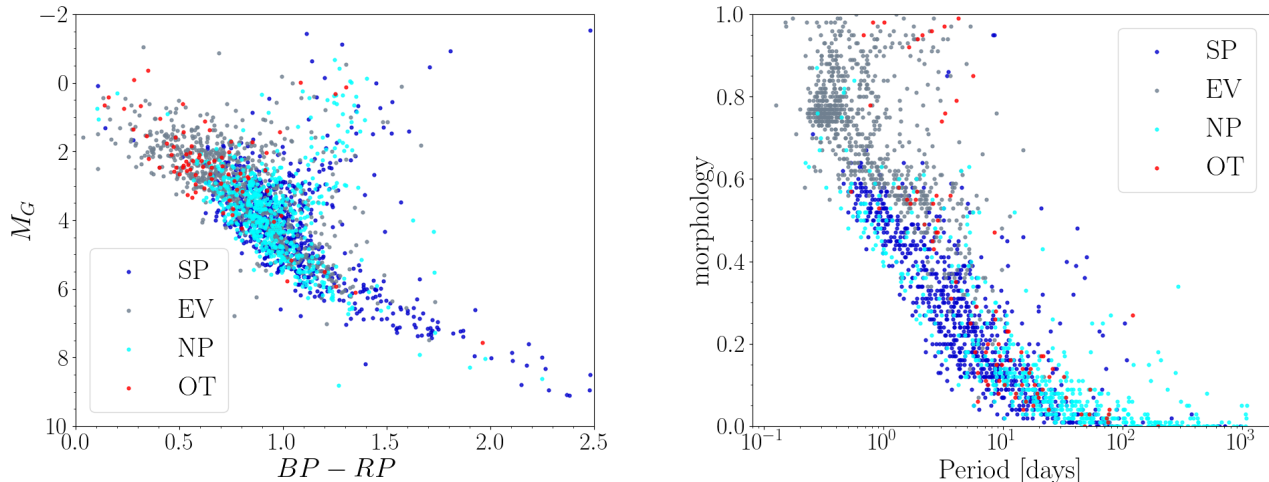
amplitude	Half the difference between the maximum and minimum magnitude
$BP - RP$	<i>Gaia</i> color from BP - RP photometry
flux percentile ratio mid 20	(60 flux percentile - 40 flux percentile) / (95 flux percentile - 5 flux percentile)
flux percentile ratio mid 35	(67.5 flux percentile - 32.5 flux percentile) / (95 flux percentile - 5 flux percentile)
flux percentile ratio mid 50	(75 flux percentile - 25 flux percentile) / (95 flux percentile - 5 flux percentile)
flux percentile ratio mid 65	(82.5 flux percentile - 17.5 flux percentile) / (95 flux percentile - 5 flux percentile)
flux percentile ratio mid 80	(90 flux percentile - 10 flux percentile) / (95 flux percentile - 5 flux percentile)
$G_{\text{mag}}$	<i>Gaia</i> G absolute magnitude
mean absolute deviation	Median absolute deviation (from the median) of the observed values
morph	light curve morphology metric (Matijević et al. 2012) quantifying how detached systems are
percent difference flux percentile	Difference between the 95th and 5th flux percentiles as a percentage of the median value
percent beyond 1 std	Percentage of values more than 1 standard deviation from the weighted average
period	Orbital period measured from Prsa et al. (2021)
period fast	Period determined from simple sinusoidal fit
std	Standard deviation of flux distribution
stetson j	Robust variance metric
stetson k	Robust kurtosis statistic
skew	Skewness of flux distribution
weighted average	Arithmetic mean of observed values, weighted by measurement errors
RUWE	<i>Gaia</i> Renormalised Unit Weight Error; astrometric goodness-of-fit

Figure 3 shows where the classifications are clustered on a *Gaia* color-magnitude diagram (left panel) and period vs. morphology plot (right panel). Here we see how the four EB classifications (SP, EV, NP, OT) fall in the two-dimensional parameter space. From the color-magnitude diagram, it is difficult to visually distinguish between the four classifications. More statistical features (e.g. Table 1) can provide additional information to separate different forms of variability and improve the accuracy of classification. However, high dimensions of features can become difficult to visualize and cumbersome to interpret and classify, motivating the use of an automated machine learning approach.

Machine learning has widely been successful in automating the classification of different types of stellar variability (and other astrophysical variability) that is observable in photometric time series (Richards et al. 2011; Kim & Bailer-Jones 2016; Jayasinghe et al. 2018). Given a well-classified sample of light curves, studies such as Jayasinghe et al. (2018) have shown that light

curve feature extraction and random forest (RF) classification are effective at distinguishing eclipsing binaries from other forms of astrophysical variability, as well as differentiating detached binaries from contact binaries. For this reason, we chose the RF method among the many machine learning classifiers. A detailed comparison of different classification methods on stellar variability is beyond the scope of this paper (see Yu et al. 2021, for a comprehensive review).

Our classification of the *TESS* EB sample consisted of two steps: an initial classification using machine learning, followed by human vetting. Training was performed by extracting features from *Kepler* lightcurve data, and then applied to features extracted from *TESS* light curve data. This involved training a RF classifier on *Kepler* lightcurves of EBs with known labels from L17, then applying the RF classifier to previously unclassified *TESS* EBs. Although the machine classifier provided mostly accurate classifications, it was limited by potential differences of extracting features from two different sur-



**Figure 3.** *Gaia* color-magnitude diagram and orbital period vs. morphology of classified *Kepler* EBs from L17. We used this catalog of *Kepler* EBs to train a random forest classifier, which we then applied to classify lightcurves from *TESS* (Section 3.1).

veys (e.g., different cadence, noise, and systematics). To more thoroughly inspect for catalog purity, we followed up with a vetting phase in which we manually inspected and validated each light curve in the sample.

For both *Kepler* and *TESS* EB samples, we compute statistical features of each light curve and cross-match the samples with *Gaia* DR3 (Collaboration et al. 2022), resulting in a sample of 2182 *Kepler* EBs with known classifications, and 3684 *TESS* EBs with unknown classifications. To compute the statistical features from the light curves we used the Python package *cesium* (Naul et al. 2016). A description of the 20 features included in our classifier is summarized in Table 1.

For the training procedure, we randomly divided the sample of 2182 *Kepler* EBs into *training sample* with 65% of the sources ( $N_{\text{train}} = 1418$ ), and a *test sample* with the remaining 35% of the sources ( $N_{\text{test}} = 764$ ). To choose the hyperparameters of the random forest classifier and avoid overfitting the model, we subdivided the training sample of 1418 sources and performed a 5-fold cross-validation test (Yates et al. 2022). From the cross-validation test, we set the number of random forest estimators to ( $N_{\text{estimators}} = 128$ ), which when applied to the test sample of 764 sources, achieved a test-sample accuracy of 85%. The confusion matrix plotted in Figure 4 shows the accuracy breakdown for each of the four classes of EBs. Figure 5 shows the relative importance of each feature described in Table 1.

We further thoroughly inspected the entire sample by visually vetting each light curve by at least two people. Figure 6 shows the classifications after human vetting. This visual verification procedure left a sample of 1039 candidate SP EBs.

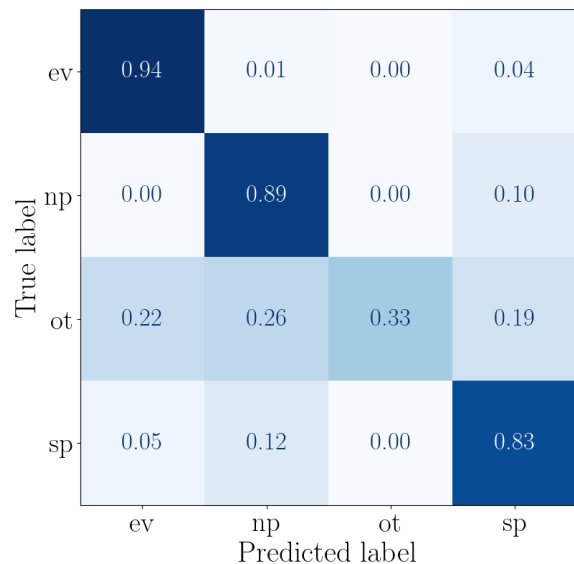


**Figure 4.** Confusion matrix evaluating the accuracy of our random forest classifier trained on labels of eclipsing binaries classified by L17. Each light curve is classified according to 4 categories: ellipsoidal variability (ev), non-periodic (np), other variability (ot), and starspot variability (sp). The y-axis shows the true label (as classified by L17) and the x-axis shows the label predicted by the random forest classifier. Entries along the diagonal of the matrix represent the percentage of sources that were accurately labeled out of the total number of true labels in each category.

### 3.2. Period Measurement

To measure rotational periods, we use the Lomb-Scargle (LS) periodogram, autocorrelation function

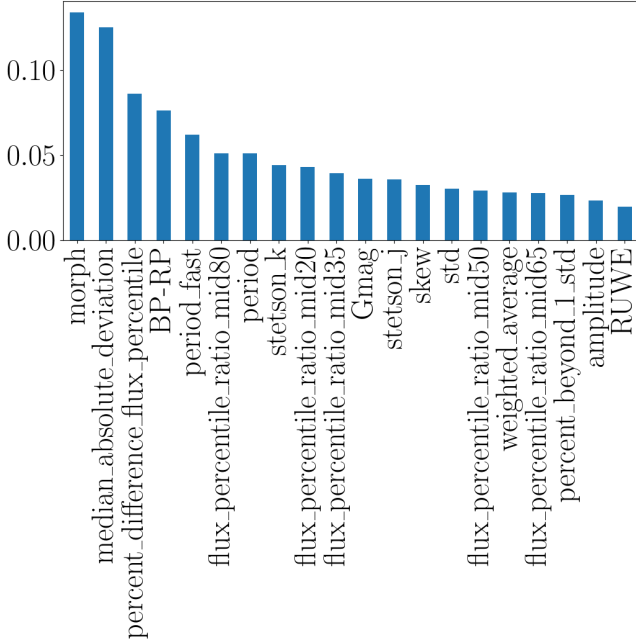


**Figure 5.** Random forest feature importance with descriptions of each feature given in Table 1.

Human classification	ev	np	ot	sp	unc
ev	1396	0	3	27	
np	106	34	19	375	
ot	69	9	13	53	
sp	341	5	28	665	
unc	316	6	23	224	
	ev	np	ot	sp	
	Random Forest				

**Figure 6.** Classes predicted by the random forest classifier compared to the human verified classifications.

(ACF), and phase dispersion minimization (PDM) function. The LS periodogram calculates the normal Fourier power spectrum and uses the least squares method to determine the best measure of the period (Lomb 1976). The LS method is advantageous in that it is efficient to compute for dense time-series and applicable to unevenly sampled data. However, LS also assumes that the time-series signal can be decomposed as a summation of

sinusoidal signals, which does not always perform well at representing the morphology of the eclipsing or star spot variability. For this reason, we also apply two other period-finding algorithms.

The autocorrelation function (ACF) for signal processing calculates the autocorrelation coefficient at time lag  $k$  for time series  $x_i$ , written in Equation (1) (Shumway 2010) as

$$ACF_k = \frac{\sum_{i=1}^{N-k} (x_i - \bar{x})(x_{i+k} - \bar{x})}{\sum_{i=1}^N (x_i - \bar{x})^2}. \quad (1)$$

Where the maximum peak in ACF values should correspond to the rotational period. ACF is advantageous when the amplitude and phase of photometric modulation significantly evolve in observations because the period remains detectable. However, long-term trends and discontinuities in a light curve introduce power at low frequencies, which can affect the ACF behavior for large lags (McQuillan et al. 2013). In our data, this resulted in aliasing within the ACF peaks, leading to peaks where the period was doubled or halved. As a result, we opted for visual selection rather than solely relying on the assumption that the first peak always represents the rotational period.

The phase dispersion minimization (PDM) approach (Stellingwerf 1978) is a nonparametric method in which the period is estimated by minimizing the scatter for the phase-folded light curve. Our implementation for PDM works as follows. First, we detrend long-term (non-rotational) variability signals using a low-order polynomial fit (Welsh 1999). The light curve is then phase-folded on a trial period  $P_0$ , where  $\phi(P_0)$  denotes the phased flux. Next the phase-folded light curve is smoothed using a rolling median function centered at the  $i^{th}$  timestep with a width  $w$ , which is computed as  $\phi_{\text{median}}(t_i, P_0) = \text{median}(\phi(t_{i-w}, P_0), \dots, \phi(t_{i+w}, P_0))$ . Next we compute the scatter between the flux and the median curve, and optimize for the period which minimizes the weighted scatter:

$$P_{\text{pdm}} = \underset{P_0}{\text{argmin}} \sum_{i=0}^N \left( \frac{\phi(t_i, P_0) - \phi_{\text{median}}(t_i, P_0)}{\sigma_i} \right)^2. \quad (2)$$

As the PDM method is computationally expensive to perform for densely sampled time series, we do not compute the phase dispersion for a wide range of trial periods. Instead, we initialize the trial period using the visually inspected LS or ACF period and use PDM to improve the precision of the period. Optimization of the weighted scatter, Equation (2), is performed numerically using `scipy.optimize`.

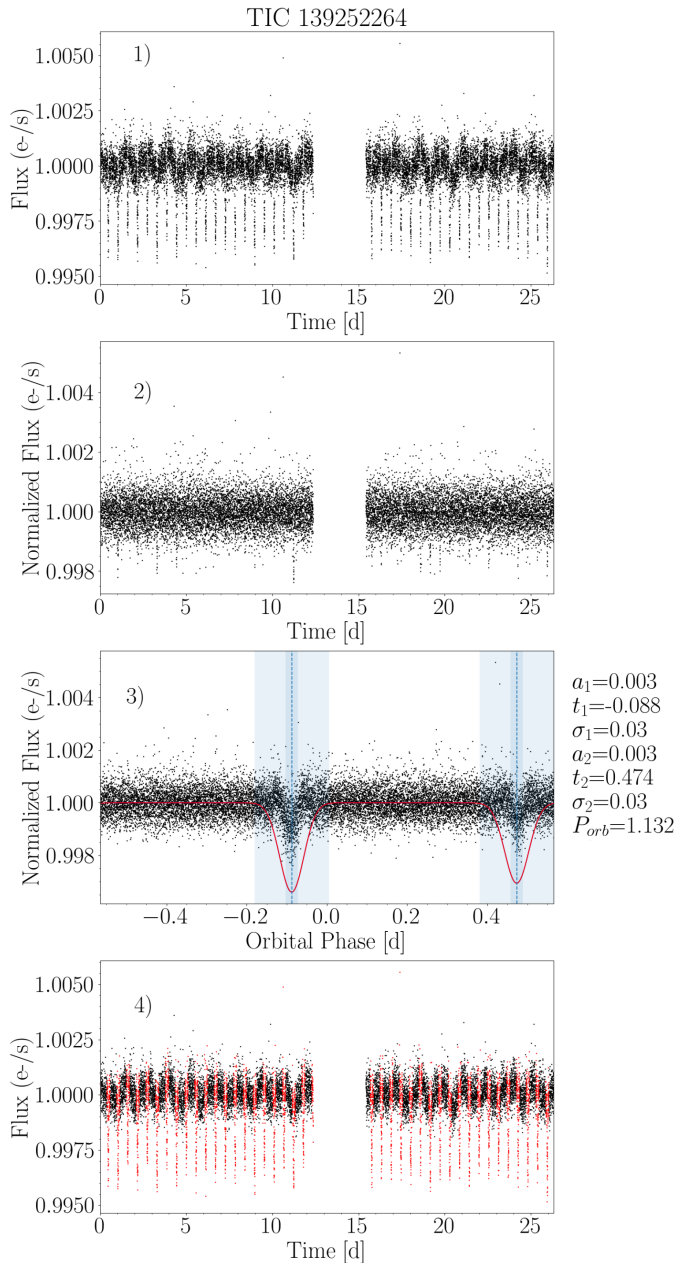


**Figure 7.** Example of a light curve with verified eclipses and masked-out data points. The top plot is the original light curve. The second is the normalized light curve. The third shows the phase-folded light curve at the optimized orbital period, where the eclipses are modeled with Gaussian functions and then subtracted from the original light curve to create the mask. The fourth shows the original light curve with the mask applied to the eclipses (red dots).

### 3.3. *TESS* Light Curves

We analyze light curves in sectors 1-26 of the *TESS* survey from the Prsa et al. (2021) catalog, and used `lightkurve` to download all sectors of the data from the *TESS* SPOC pipeline (Figure 7, Panel 1). To extract

eclipse variation, we detrend the rotational variability by normalizing the light curve with the `lightkurve` `flatten` function, which splits the light curve into segments and individually applies the `SciPy` `savgol_filter` (Figure 7, Panel 2). Once normalized, we then phase-folded the light curves on the orbital periods listed in Prsa et al. (2021), using the `lightkurve` `fold` method (Figure 7, Panel 3). With these light curves, we were able to map models of each binary star’s eclipse by fitting Gaussian models to dips in the flux from the eclipses of both stars in the binary system (Mowlavi et al. 2017). The phase-folded flux value for the eclipses was calculated using Equation (3). Where  $i$  indicates the primary ( $i = 1$ ) or secondary ( $i = 2$ ) eclipse,  $A$  is the amplitude of the dip in phase-folded flux,  $t$  are the time values in the phase-folded light curve,  $t_{\min}$  is the time of the dip’s minimum, and  $d$  is the duration of the dip in days:

$$y = A_i \cdot \exp \left[ -(t - t_{\min,i})^2 / (2d_i^2) \right]. \quad (3)$$

We used the minimum of the phase-folded light curve flux values to obtain the primary eclipse amplitude ( $A_1$ ) and the time at the minimum ( $t_{\min,1}$ ). This technique was repeated to identify the second minimum, resulting in the secondary eclipse’s amplitude ( $A_2$ ) and time at the secondary minimum ( $t_{\min,2}$ ). In this initial optimizer, the duration ( $d_1$  and  $d_2$ ) for both eclipses was set to the same fixed value (typically 0.03 days) and  $t_{\min,2}$  was assumed to be within 0.25 days in phase of  $t_{\min,1}$ . These estimations were adjusted manually, if required, after an inspection of an over-plot of the eclipse models on the phase-folded light curve. We ran these parameters through a second optimizer that minimized  $\chi^2$  through the least squares method in the bounds of the phase-folded light curve. This yielded our final parameters for the eclipse models, as well as an optimized orbital period (Figure 7, Panel 3).

With the optimized parameters, we then mask the overlap of the eclipse models on the original data, which removes the flux measurements during eclipses that creates high scatter in phase-folded light curves that are not folded on the orbital period. To remove the eclipse signals from the light curves, we used a duration mask of  $\pm 3$  standard deviations from the mean of the Gaussian fit. This mask was made using the eclipse mask of `BoxLeastSquares` using the eclipse times ( $t_{\min,1}$  and  $t_{\min,2}$ ), the best-fit orbital period (obtained from LS, ACF and PDM in Section 3.2), and the eclipse duration ( $d_1$  and  $d_2$ ). Two masks (one around each eclipse at  $t_{\min,1} \pm 3d_1$  and  $t_{\min,2} \pm 3d_2$ ) were made and applied to each of the data arrays for time, flux, and error. These masks are the red scatter values in Figure 7, Panel 4.

### 3.4. Measurement Procedure Rotational Periods

After measuring the orbital periods using the model in 3.2, we then measure the rotation periods. First, we mask out the eclipses from the light curve using the eclipse timings and durations from our transit model fit 3. Next, we applied both Lomb-Scargle and ACF to the masked light curve to measure the rotation period as described in the Methods Section 3.2. In cases where the highest peak in the ACF did not look like the rotational period, we manually specify the peak to the ACF (Figure 8, Panel 1). In the event that neither of the LS or ACF measurements appears correct, we also apply PDM. In the PDM, we use the results of the rotational period of the LS and ACF methods as an initial guess (Figure 9, Panel 1). In the event that neither LS nor ACF is a good initial guess, we use a manual guess by visually inspecting the original light curve for an estimation.

To visualize whether any of these values represented the correct rotational period, we plot phase-folded light curves (Figure 7, Panel 5; Figure 8 Panel 2; Figure 9, Panel 2) and visually inspected these plots for each method. The rotational period value that produces the most periodic-looking single phase among the methods is saved as the rotational period for the TIC ID. There were outlier cases where the phase-folded light curve did not appear periodic or suggested the presence of an n-body system. We discarded these outliers from our sample catalog because we were unable to identify a rotational period using our described methods (Section 3.2).

### 3.5. Bayesian model comparison

Next, we analyze the  $P_{\text{orb}}/P_{\text{rot}}$  distribution of the sample and use Bayesian model comparison to quantify the significance of the second subsynchronous peak discovered in L17. To do this, we calculated whether a double-peaked model was a significantly better fit than a single-peaked model. Given that we do not have a theoretical model for the spin-orbit distributions (and as discussed in the results, the empirical distributions are roughly symmetric), we chose to fit each distribution using a combination of either Gaussian or Lorentzian functions. In particular, we evaluated four models: single Gaussian, double Gaussian, single Lorentzian, and double Lorentzian. For the models, we use the `scipy` norm and cauchy functions with the `cdf` method for a single Gaussian and Lorentzian, respectively. The double peak models consisted of two of the same functions, the second of which had an amplitude parameter, which were summed and normalized.

Rather than using a histogram, which may miss the intricacies of the data, we chose Kernel Density Estima-

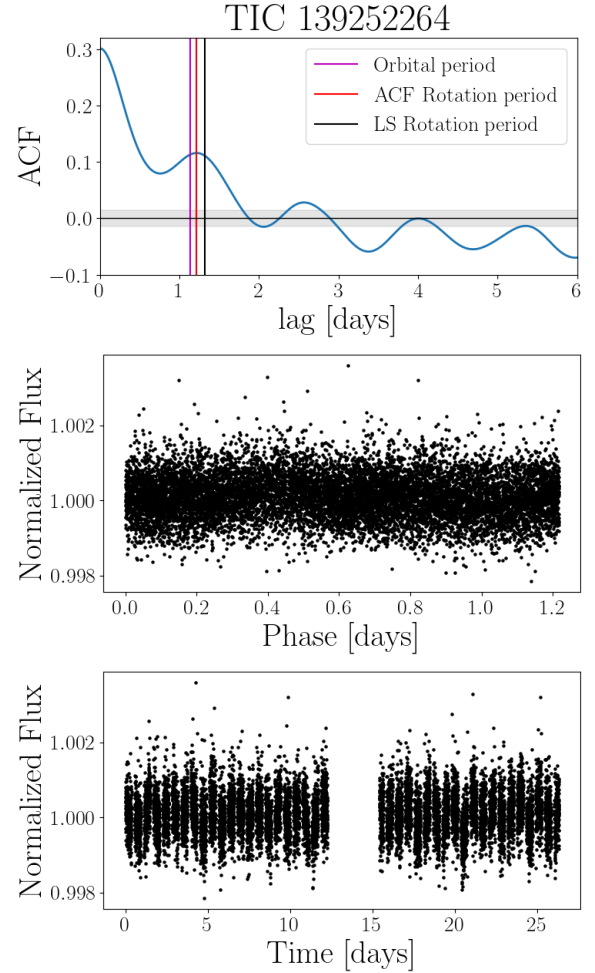


**Figure 8.** Example of a light curve with an applied mask on the orbital period and eclipses, used with the autocorrelation function (ACF) to identify the rotational period. The first plot is the ACF periodogram, with the orbital period, LS rotational period, and ACF rotational period marked. The second is the light curve phase folded on the ACF period. The third as the original light curve with eclipses masked out.

tion (KDE) to estimate a Probability Density Function (PDF). Using `GridSearchCV` from the package `sklearn` and 20-fold cross-validation to ensure low coefficient variability, we calculated the ideal bin width for the KDE yielding a smoothed PDF. Following that, we normalize the PDF by dividing it by its sum of values.

The challenge with using a KDE is that its effectiveness depends heavily on the chosen bin width. Over-smoothing may occur with a large bin width, while a small width may result in under-smoothing. Despite KDE’s ability to provide useful PDF visualizations, we decided to convert the sample into an estimated Cumulative Density Function (CDF) because it is derived entirely from the data sample, which eliminates worries

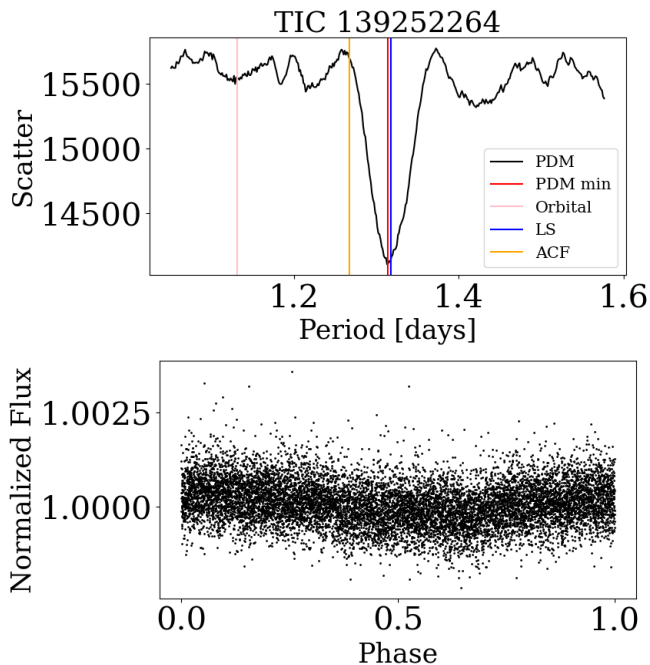


**Figure 9.** Example of a light curve of TIC ID 139252264 with an applied mask on the orbital period and eclipses, used in conjunction with phase dispersion minimization (PDM) to identify the rotational period. The first plot shows a PDM periodogram comparison, with the orbital period, LS rotational period, and ACF rotational period marked. The second displays the light curve phase-folded on the PDM identified rotational period.

about artificial feature generation or manipulation that might impair model fitting. The CDF function was calculated by dividing the cumulative total of unique spin-orbit ratios by their sum. To test whether it is plausible that the *Kepler* and *TESS* samples originate from the same underlying distribution, we perform a two-sample Cramér-von Mises test (Anderson 1962) with the null hypothesis that the two populations are identical. Applying this test to the two CDF functions, we compute an output p-value of 0.99, indicating that we cannot reject the null hypothesis. This test suggests that the samples originate from the same underlying distribution. To evaluate the statistical significance of the subpopulation, we modeled the *TESS*, *Kepler*, and combined data samples.

To identify optimal model fits, we implement a Bayesian sampling approach using the *dynesty* *NestedSampler*. We sample the combined data using the natural log-likelihood of both single- and double-peaked Gaussian and Lorentz CDFs, with each sampler assuming a uniform prior (given the ranges in Table 2). Since the measurement error for the orbital and rotational periods is unknown, we apply a uniform error of

Parameter	Minimum	Maximum
$\mu_1$	0.9	1.1
$\sigma_1$	0.01	.5
$\gamma_1$	0.001	.5
$\mu_2$	0.7	0.9
$\sigma_2$	0.01	0.05
$\gamma_2$	0.01	0.05
$a$	0.1	1

**Table 2.** The ranges for Gaussian and Lorentzian parameters, listed with the minimum and maximum for the ranges. The parameters are  $\mu_1$  (primary mean),  $\sigma_1$  (primary standard deviation),  $\gamma_1$  (half width half maximum),  $\mu_2$  (secondary mean),  $\sigma_2$  (secondary standard deviation),  $\gamma_2$  (half width half maximum),  $a$  (secondary amplitude). The primary amplitude is always 1, so it is not included as a parameter.

0.025 to all spin-orbit ratios in the likelihood functions, which is equivalent to the standard deviation of a single Gaussian KDE on the *TESS* data. We opt for a uniform error because we do not have an informed guess as to what the true distribution of non-uniform errors is. A uniform error captures a non-precise estimate of how the minimum and maximum error cases would impact our models. For our four different models,  $Y$  (single Gaussian, double Gaussian, single Lorentzian, and double Lorentzian), we calculated the natural log-likelihood of the model fit as:

$$\ln \mathcal{L}(Y|\theta) = -\frac{1}{2} \sum_{i=1}^N \left[ \frac{Y(x_i) - C(x_i)}{\sigma} \right]^2 - 2N \ln \sigma, \quad (4)$$

where  $x_i = P_{\text{orb}}/P_{\text{rot}}$  is the spin-orbit ratio,  $C(x_i)$  is the CDF of the data as a function of spin-orbit ratio,  $Y(x_i)$  is the model fit, and  $\sigma$  is the error for the observations  $x_i$ . One limitation of the period measurement methods we employed (Lomb-Scargle, autocorrelation function, and phase dispersion minimization, Section 3.2) is that it is difficult to accurately determine the uncertainty of the period measurement. We estimate a fiducial error of  $\sigma = 0.025$ , based on the standard deviation of sources around the 1:1 spin orbit ratio (assuming that most sources around 1:1 are synchronized and the dispersion around 1:1 is mostly due to measurement error). However, since this value for  $\sigma$  is only a rough estimate, when we later test the significance of the Bayes factor as a function of error (mentioned at the end of this section) by varying the error values between the range of  $\sigma = 0.01 - 0.5$ .

The bimodal posteriors include an amplitude parameter to scale to the secondary peak observed in the subsample. The ranges for the parameters are listed in Ta-

ble 2. It should be noted that for the single Lorentz we changed the range of  $\gamma_1$  to have a maximum of 0.02, because the sampler made  $\gamma_1$  much too large when sampling.

To assess which posterior best aligns with the combined data, we computed the Bayes factors, representing the marginal likelihood ratio of two different models (Kass & Raftery 1995).

The marginal likelihood (or evidence)  $Z$  is computed by integrating the model likelihood over the prior:

$$Z = P(D|M) = \int P(D|\theta, M) P(\theta|M) d\theta, \quad (5)$$

where  $D$  is the data and  $M$  is a given model with parameters  $\theta$ .  $\theta$  represents the set of model parameters for each of the four models (Table 2):  $\theta_{sg} = \{\mu, \sigma\}$  for single Gaussian,  $\theta_{dg} = \{\mu_1, \sigma_1, \mu_2, \sigma_2, a\}$  for double Gaussian,  $\theta_{sl} = \{\mu, \gamma\}$  for single Lorentzian, and  $\theta_{dl} = \{\mu_1, \gamma_1, \mu_2, \gamma_2, a\}$  for double Lorentzian. Subsequently, the natural log-marginal likelihood was utilized in Equation (6) to compute the natural log Bayes factor,

$$\mathcal{B} = \frac{Z_1}{Z_2}, \quad (6)$$

$$\ln \mathcal{B} = \ln Z_1 - \ln Z_2.$$

The results of our model comparison test are discussed in Section 4.5.

**Table 3.** Columns of Catalog

TIC	<i>TESS</i> object ID
primary eclipse amplitude	flux amplitude of the primary eclipse
primary eclipse time	time in days on a single phase where the primary eclipse occurs
primary eclipse duration	duration in days of the primary eclipse
secondary eclipse amplitude	flux amplitude of the secondary eclipse
secondary eclipse time	time in days on a single phase where the secondary eclipse occurs
secondary eclipse duration	duration in days of the secondary eclipse
orbital period	orbital period in days that has been run through an optimizer
LS rot. period	rotational period in days found using the Lomb-Scargle method
flag note	notes about issues encountered with the TIC ID
rotation period inspected	rotational period in days from visual inspection
ACF rot. period	rotational period in days found using the autocorrelation function
	rotational period in days found using phase dispersion minimization
synch	value of orbital period / rotation period inspected
alias period	period that was identified in at least one method as being the rotational period, but was within a half or double increment of the inspected period
eccentricity	$\text{ecos}(\omega)$
nsectors	number of sectors used when calculating the LS and ACF rotational periods
PDM Scatter	saved scatter value of the phase dispersion minimization method for the resulting PDM rot. period

## 4. RESULTS

In this section, we give a brief overview of our rotation period catalog and the subsample of EBs classified with starspot rotation. We then use this subsample to inspect the synchronization trend of EBs classified with starspot rotation.

### 4.1. Rotation Period Catalog

Table 3 lists the column titles and their descriptions for our rotational period catalog. The full catalog is available in the online supplement. We provide the eclipse and duration parameters along with the orbital period needed to mask out eclipses from the *TESS* light curve. We also include all measurements of the rotational period across methods and separately list the rotational period we use in our analysis (rotation period inspected).

### 4.2. Starspot Rotation subsample

To ensure confident calculation accuracy of a system’s rotational period, we created a subsample of EBs classified as starspot rotation, comprising 584 TIC IDs. To fit the orbital period, we used all sectors of data with the TIC IDs. We then used the methods described in Section 3 to obtain a fitted value for the orbital period, LS rotational period, and ACF rotational period. We initially used a single sector of data, and then used full-sector data for EBs with orbital periods  $>6$  days.

We opted not to employ the PDM rotational method for the full-sector data due to the extensive calculation time required. Instead, we used data solely from the first sector for PDF rotational periods. The inspected rotational period compares the full sector ACF and LS periods with the single sector PDM period. The period with the lowest scatter and most obvious rotation period by visual inspection was saved as the inspected period.

Our visual inspection consisted of comparing the phase-folded light curves for each method of rotation period measurement. If the scatter values across methods were similar (showing no significant differences in the first 3-5 orders of magnitude) we made a judgment based on the most apparent rotational period. For example, when one phase-folded light curve appeared jagged, flat, or noisy, while another displayed a relatively smooth curve, we selected the rotational period associated with the smoother curve.

To analyze the degree of synchronization for a given EB, we calculate the spin-orbit ratio of  $P_{\text{orb}}/P_{\text{rot}}$ . Synchronization occurs at  $P_{\text{orb}}/P_{\text{rot}} = 1$ ; where  $P_{\text{orb}}/P_{\text{rot}} < 1$  is subsynchronous, and  $P_{\text{orb}}/P_{\text{rot}} > 1$  is supersynchronous. For our subsample, 88% of the EBs have period ratios in the range of 0.75 to 1.25. To ensure accurate results, we recomputed the rotational and orbital periods for TICs using full sector data that fall within the subsynchronous range we are looking for (approximately  $0.82 < P_{\text{orb}}/P_{\text{rot}} < 0.92$ ). This ratio is used

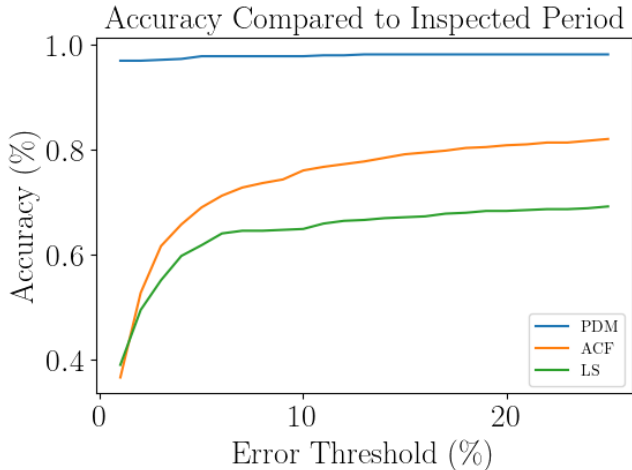


**Figure 10.** Plot of each method’s level of accuracy against an error threshold range of 1-25%. The error is the root mean square of the difference of the method rotational period to the inspected rotational period.

throughout our figures to find significant correlations with synchronization.

#### 4.3. Comparing rotational period measurements from different methods

We evaluated the overall precision of each method using two metrics: the root mean squared error (RMSE) and 10% accuracy of the methods. The RMSE was calculated by taking the the root mean square of the difference of the inspected period and a method’s period. The root mean squared error for LS was 4.3 days, ACF was 1.5 days, and PDM was 0.2 days. This metric is strongly skewed by outliers, which are more prevalent in the LS method.

Meanwhile, 10% accuracy is less affected by outliers, and suggests which method results in higher accuracy. Examining 10% accuracy ensures that we are considering the correct period and not an alias that can result from orbital effects. When assessing how often the methods were within 10% of the inspected period, LS had 64%, ACF had 76%, and PDM had 98% of values with 10% accuracy. Figure 10 shows accuracy trends of each method for a given error threshold, with the range of error being from 1-25%. By inspecting these three methods, we found that the PDM period accounted for the majority of the inspected periods, with a prevalence of 96%.

We also compare our different methods of measuring the rotational period to see if there are any trends that bias our measurements in a method. Figure 11 compares our methods to one another in log-log space, with given ratios marked with dashed lines. Out of all the techniques, the LS method is the least accurate in that

it overestimates the rotational period, as well as often doubling the period when compared to both the ACF and inspected period. This is because Lomb-Scargle is moved out of phase as star spots evolve, making ACF overall more reliable for star spot modulated lightcurves (Gordon et al. 2021). When comparing the ACF and inspected periods, note that the inspected period largely corresponds to the PDM period, which was measured with only a single data sector. Data points with more than one sector could be more accurately measured using the ACF method. The ACF method appears to largely align with the inspected period, although there are some trends indicating doubling or halving of the rotational period.

To better understand the results, we filter our sample for the most consistent results across the methods. Figure 12 plots the period ratio of the inspected period alongside the L17 data. See Figure 20 in the Appendix for a look at the sub-sample at different confidence levels, where we see the subsynchronous secondary peak is only prominent in the consistency range of 20%. For our full sample in figure 12 the percentage of the subpopulation to the total population is 6% and emerges as a weak subsynchronous peak in the histogram. The number of systems in the subpopulation was defined as those having a spin-orbit ratio range of  $0.82 < P_{\text{orb}}/P_{\text{rot}} < 0.92$ . This percentage is significantly less than the one found in L17 of 15%, but the secondary peak confirms that the subsynchronous EB population observed in L17 is not an artifact specific to the *Kepler* instrument or survey. We can not conclude from this population percentage alone if the subsynchronous EB population is significant. To assess the significance, we combined the L17 *Kepler* data with our full *TESS* confident dataset to create a modeled sample. In this combined sample, 8% of the total population falls within the subsynchronous subpopulation.

#### 4.4. Trends Across Stellar Type and Galactic Location

To analyze the types of stars present in the subsample, we cross referenced in TOPCAT (Taylor 2005) the RA and DEC of the TICs with the Gaia catalog DR3 (Gaia Collaboration et al. 2023) within 5". Figure 13 is a color magnitude diagram of the cross-matched subsample, with a color bar of the spin-orbit ratio. This figure shows how our subsample contains primarily main-sequence stars, with a portion in the subgiant phase. There are some giant and supergiant systems present in the subsample, but there is no clear trend of synchronization with placement on the diagram.

Confident that we are primarily working with main sequence EBs, we can now map any dominant trends of

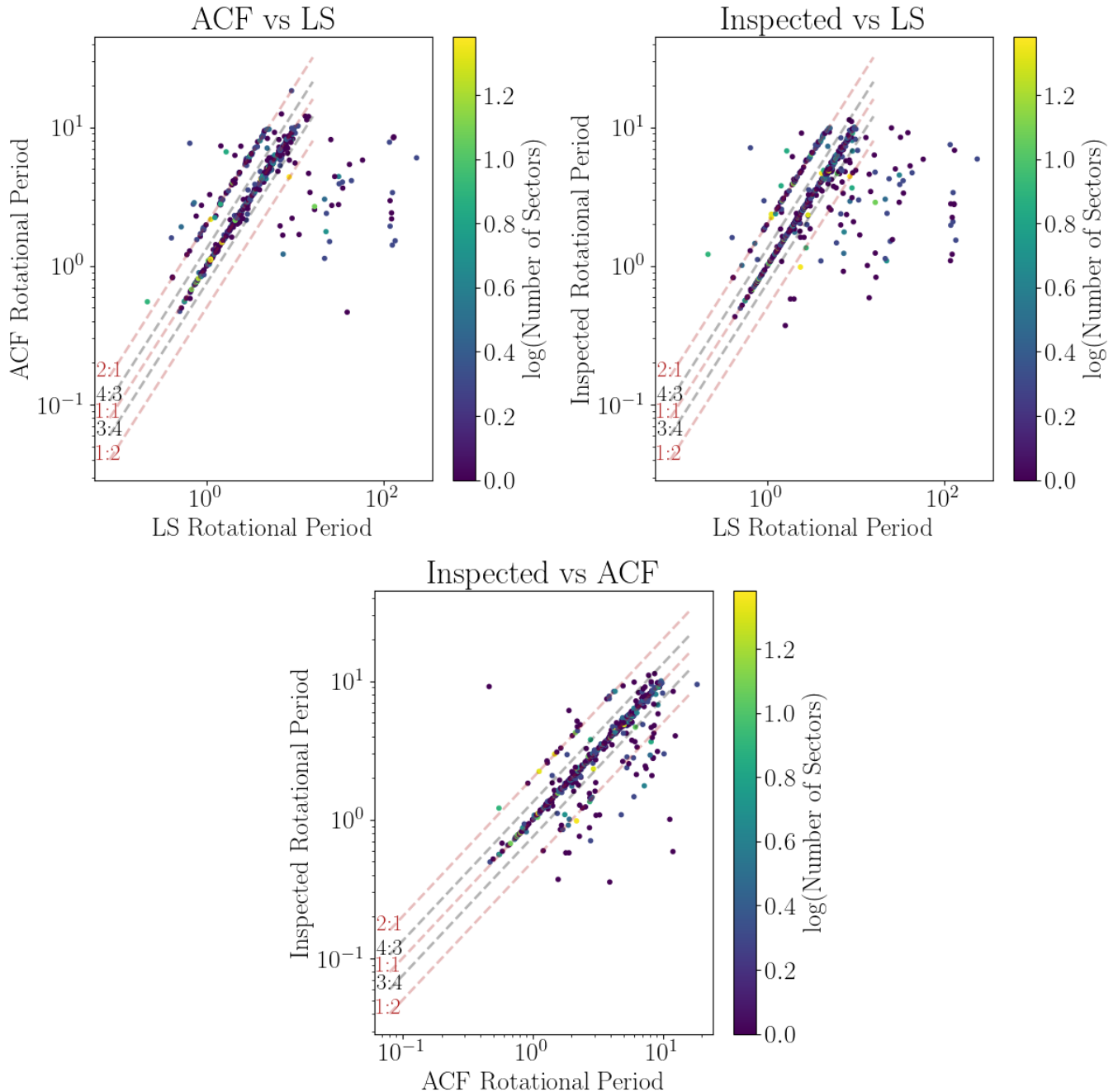


**Figure 11.** Comparison between different results of rotational period techniques. With dashed lines of common ratios.

synchronization across stellar class, using effective temperature and Table 4. Figure 14 reveals that a significant portion of our subsample are G and F stars, which is consistent with the distribution of *TESS* targets (Stassun et al. 2018). There are 116 EBs not included in this figure, due to a missing effective temperature in the cross-match ID in the catalog *Gaia*. The systems that are approximately synchronized have  $0.8 < \frac{P_{orb}}{P_{rot}} < 1.2$ , and all other ratios are categorized as not synchronized.

We conclude that all star types can be synchronized, and there is no dominate synchronized stellar class.

To cross-check that the EBs are young enough to be main-sequence stars, we check their galactic position. Figure 15 maps the EBs by their galactic kinematics. It is expected that young stars will be in the thin disk and will be older as they populate the thick disk, and very old if they are in the halo. Nearly all of the unsynchronized systems in the figure are within the thin disk and thus are young EBs. This is consistent with the knowl-

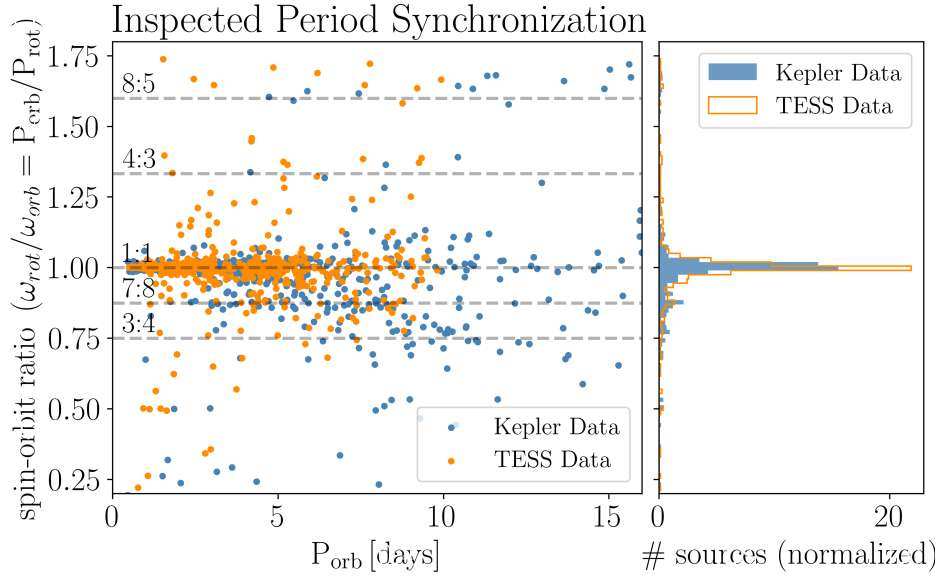


**Figure 12.** Full *TESS* sample inspected period, plotted alongside the L17 *Kepler* data.

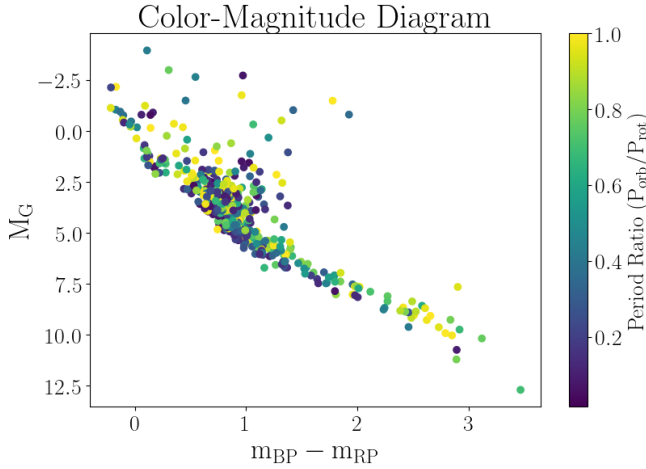


**Figure 13.** Cross matched EB catalog with *Gaia* data as a color magnitude diagram, colored by the EB's period ratio.

Class	$T_{eff}[K]$
O	$\geq 3300$
B	10,000–33,000
A	7,300–10,000
F	6,000–7,300
G	5,300–6,000
K	3,900–5,300
M	2,300–3,900

**Table 4.** Effective temperature to stellar classification.

edge that synchronization occurs over long time scales. With an understanding of the types of stars we are examining, we can compare how various rotational period

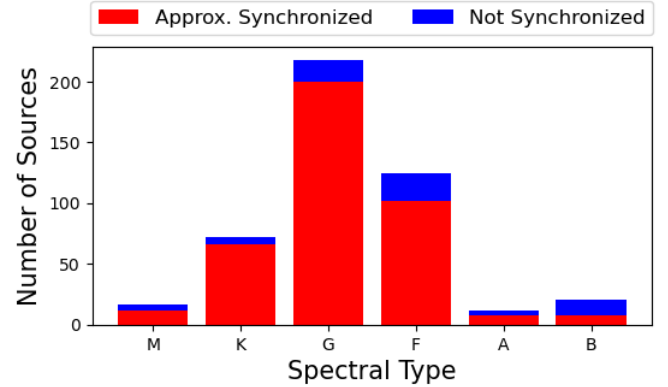


**Figure 14.** Frequency of spectral type in the catalog. Cross matched EB catalog with *Gaia* data as a stacked bar chart, by spectral type.

methods influence the spin-orbit ratio.

#### 4.5. Quantifying the significance of the synchronized population

To find the mean and median posterior parameters, we weighted each model's *NestedSampler* result. Table 5 presents the weighted mean and median parameters for all models to the respective data sets. Figures 16 and 17 show the corner plots in blue and red respectively for the combined data set. The corner plots display asymmetry, where the peak of the corner plots are similar but the width of the distributions are slightly skewed. Due to this asymmetry, we employed the median for the remainder of our figures, even though the values of the median and mean values are extremely close. Figure 18

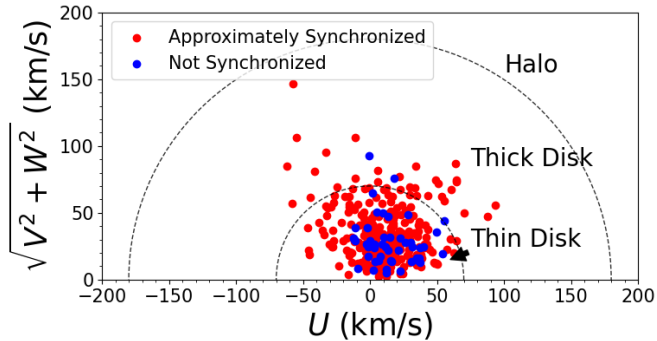


**Figure 15.** A visualization of our catalog’s galactic coordinate positions based on *Gaia* data. where  $V$  represents the velocity (km/s) in the direction of Galactic rotation,  $W$  represents the velocity (km/s) toward the North Galactic Pole, and  $U$  represents the velocity (km/s) toward the Galactic center. The majority of our catalog is contained in the Milky Way’s thin disk, which also houses almost all of the non-synchronous systems.

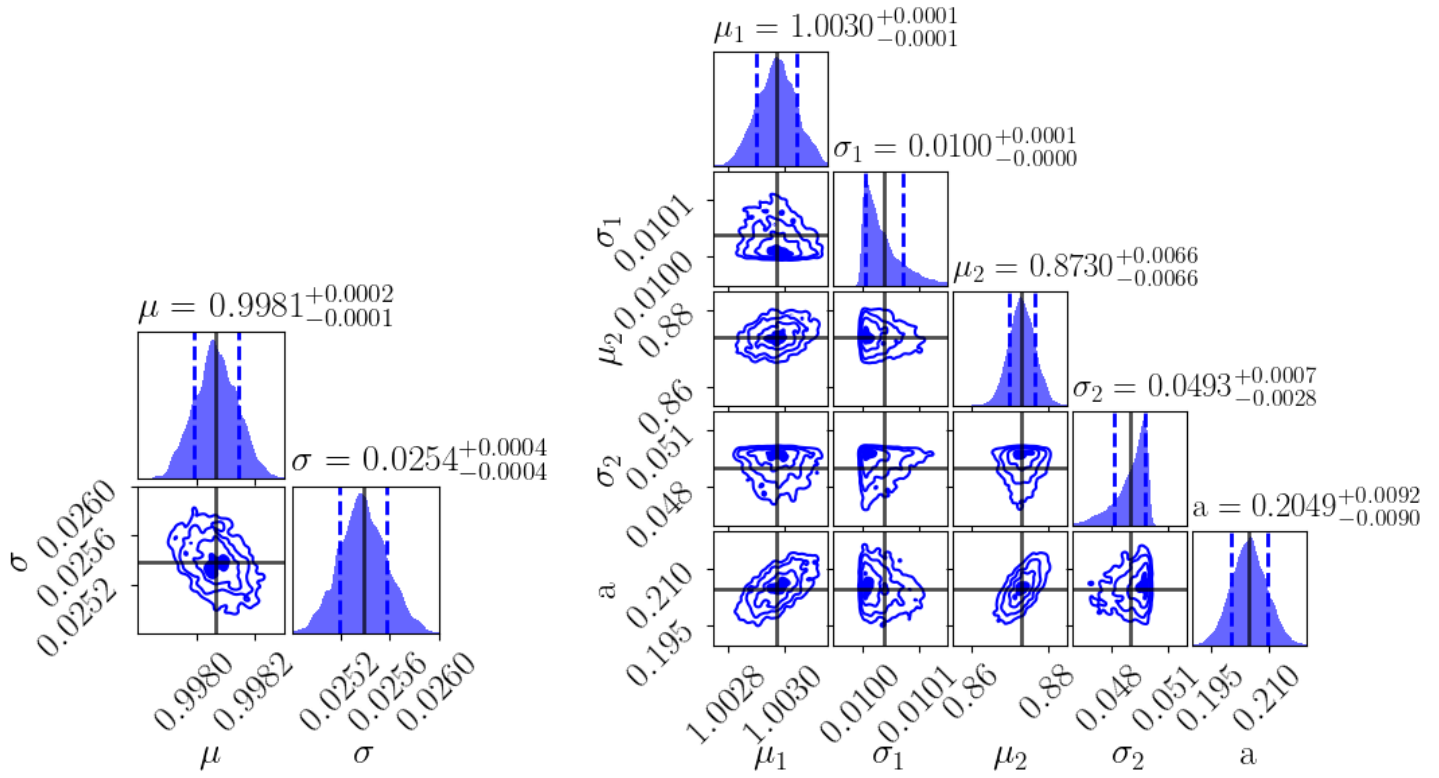
depicts the median posteriors overlaid on both the CDF and normalized PDF across datasets.

To compare these best-fit models, we calculated the natural log Bayes factors for all models. Specifically, we examined how the Bayes factors depend on the spin-orbit ratio error for two different model comparisons: a double Gaussian versus a single Gaussian, and a double Lorentzian versus a single Lorentzian. These comparisons were selected because our primary interest lies in assessing the significance of the secondary population, rather than identifying the optimal distribution type.

The significance of the natural log Bayes factor ( $\ln \mathcal{B}$ ) falls into the following ranges (Kass & Raftery 1995):  $\ln \mathcal{B} < 0$  supports  $Z_2$ ,  $0 < \ln \mathcal{B} < 1$  barely supports  $Z_1$ ,  $1 < \ln \mathcal{B} < 3$  positively supports  $Z_1$ ,  $3 < \ln \mathcal{B} < 5$  strongly supports  $Z_1$ , and  $\ln \mathcal{B} > 5$  very strongly supports  $Z_1$ .

Table 6 presents the calculated natural log Bayes factors across posteriors, demonstrating that a double-peaked distribution, is decisively the best fit across data sets. For the *TESS* data, a double distribution is the best fit, with a small favorability towards the double Lorentz. However, a double Lorentzian decisively provides the best fit for both the *Kepler* and combined data sets. However, given that our results are contingent on a rough estimate of the uncertainty of the spin-orbit ratio, we computed various natural log Bayes factors across a range of errors to assess if it would alter our conclusions. Using the same process as described in Section 3.5, we tested varying the spin-orbit ratio uncertainty between 0.01 and 0.5, in the likelihood calculations. Figure 19 shows how our confidence in model selection depends on the typical error value chosen across data points.

The dashed horizontal black lines indicate the significance levels of the Bayes factor and the solid black vertical line shows our fiducial error value of  $P_{orb}/P_{rot} = 0.025$ . This figure illustrates that, even with large error values, a double-peaked distribution remains decisively superior to a single-peaked distribution, affirming the reality of the subpopulation regardless of the true error values. At large error values, a double Gaussian is better fit, as the broad Lorentzian wings make it challenging to distinguish between a single and double distribution. See Figure 21 in the Appendix for visualization that a double Gaussian is decisively a best fit.



(a) Single Gaussian posterior corner plot.

(b) Double Gaussian posterior corner plot.

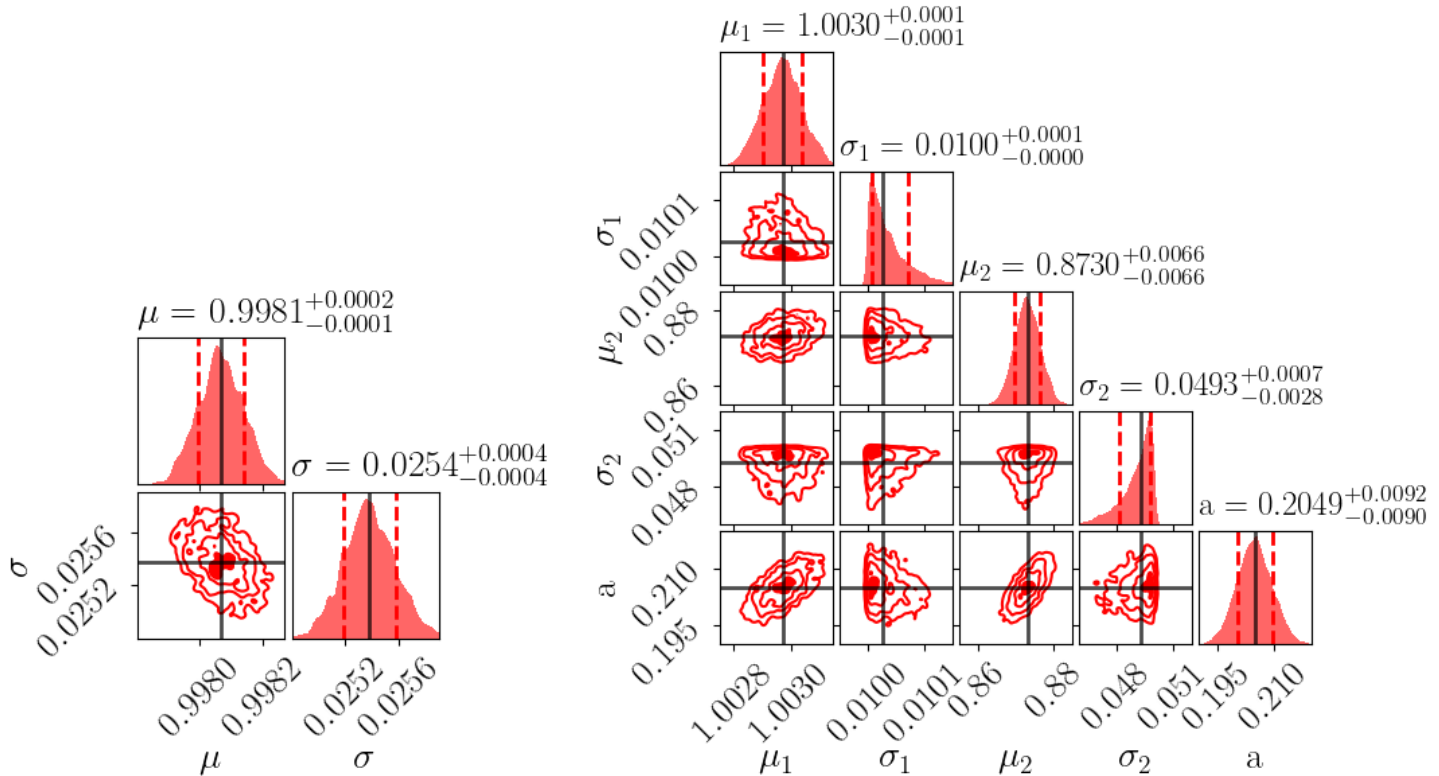


**Figure 16.** Corner plots for the weighted mean (blue) and median (red) Gaussian posteriors. The parameter values are shown with black lines. The parameters are  $\mu_1$  (primary mean),  $\sigma_1$  (primary standard deviation),  $\mu_2$  (secondary mean),  $\sigma_2$  (secondary standard deviation),  $a$  (secondary amplitude). The weighted mean consistently has values within the 5-sigma contour, while the median often does not have values within the 5-sigma bounds.

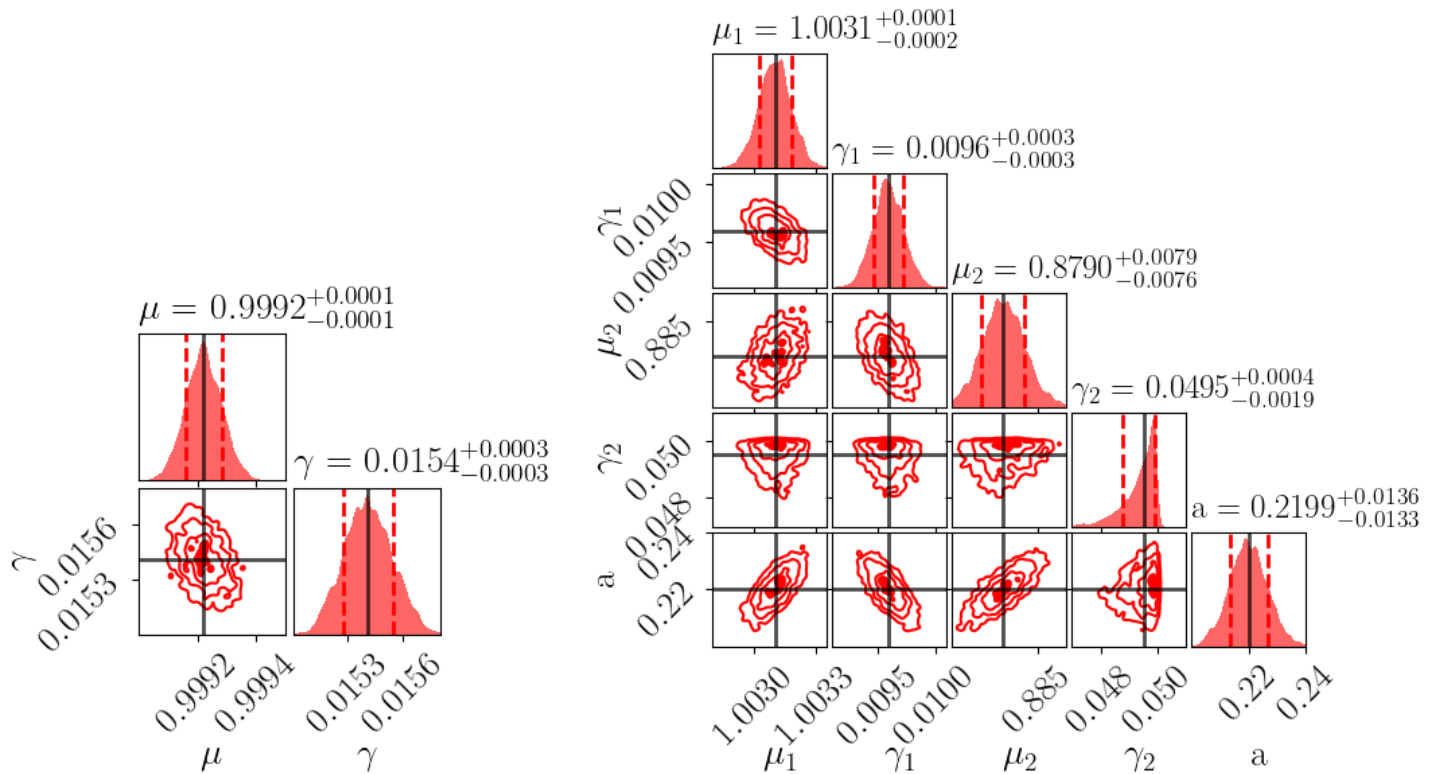
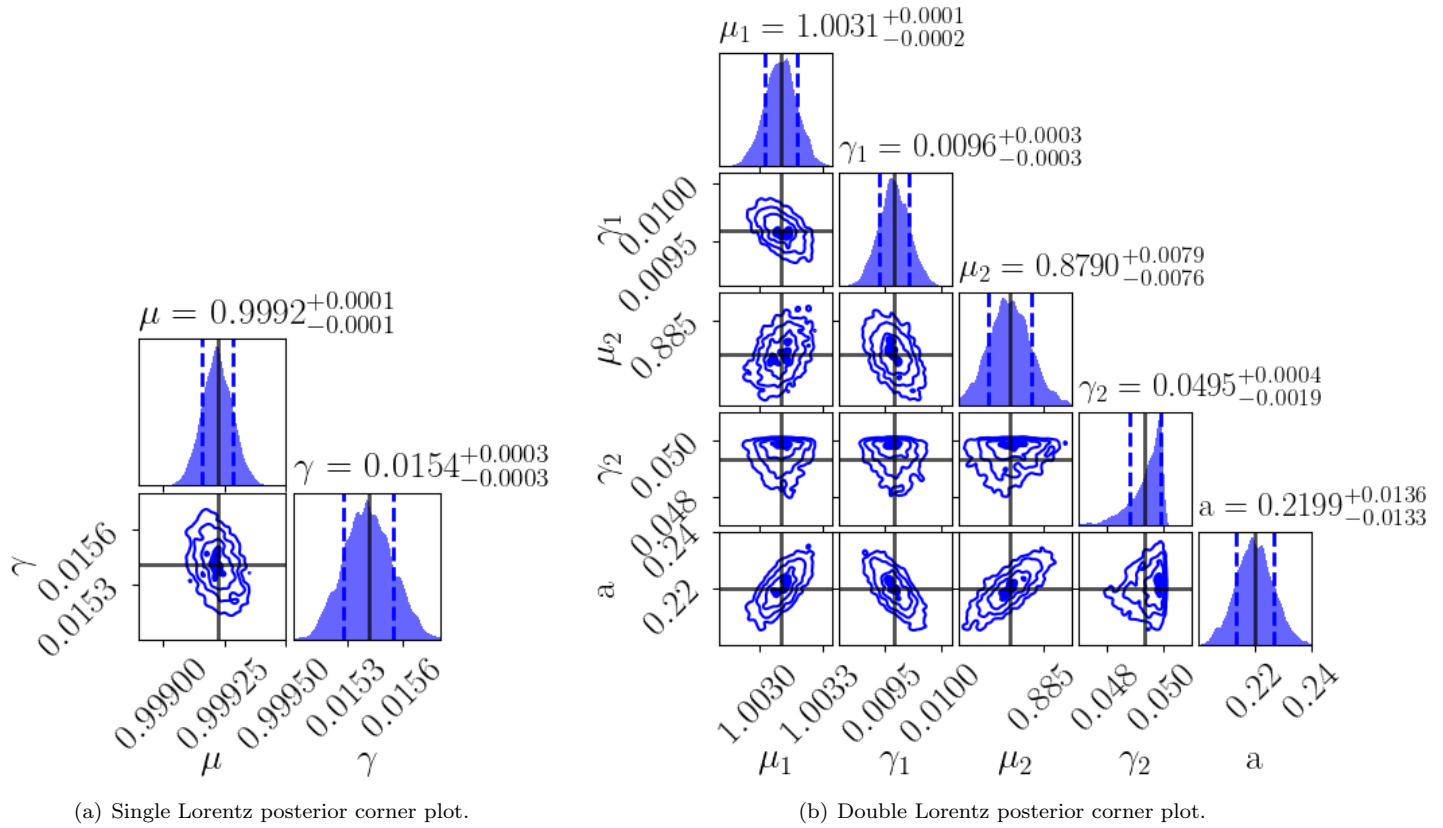


**Figure 17.** Corner plots for the weighted mean (blue) and median (red) Lorentz posteriors. The parameter values are shown with black lines. The parameters are  $\mu_1$  (primary mean),  $\gamma_1$  (primary half width half maximum),  $\mu_2$  (secondary mean),  $\gamma_2$  (secondary half width half maximum),  $a$  (secondary amplitude). The weighted mean consistently has values within the 5-sigma contour, while the median often does not have values within the 5-sigma bounds.

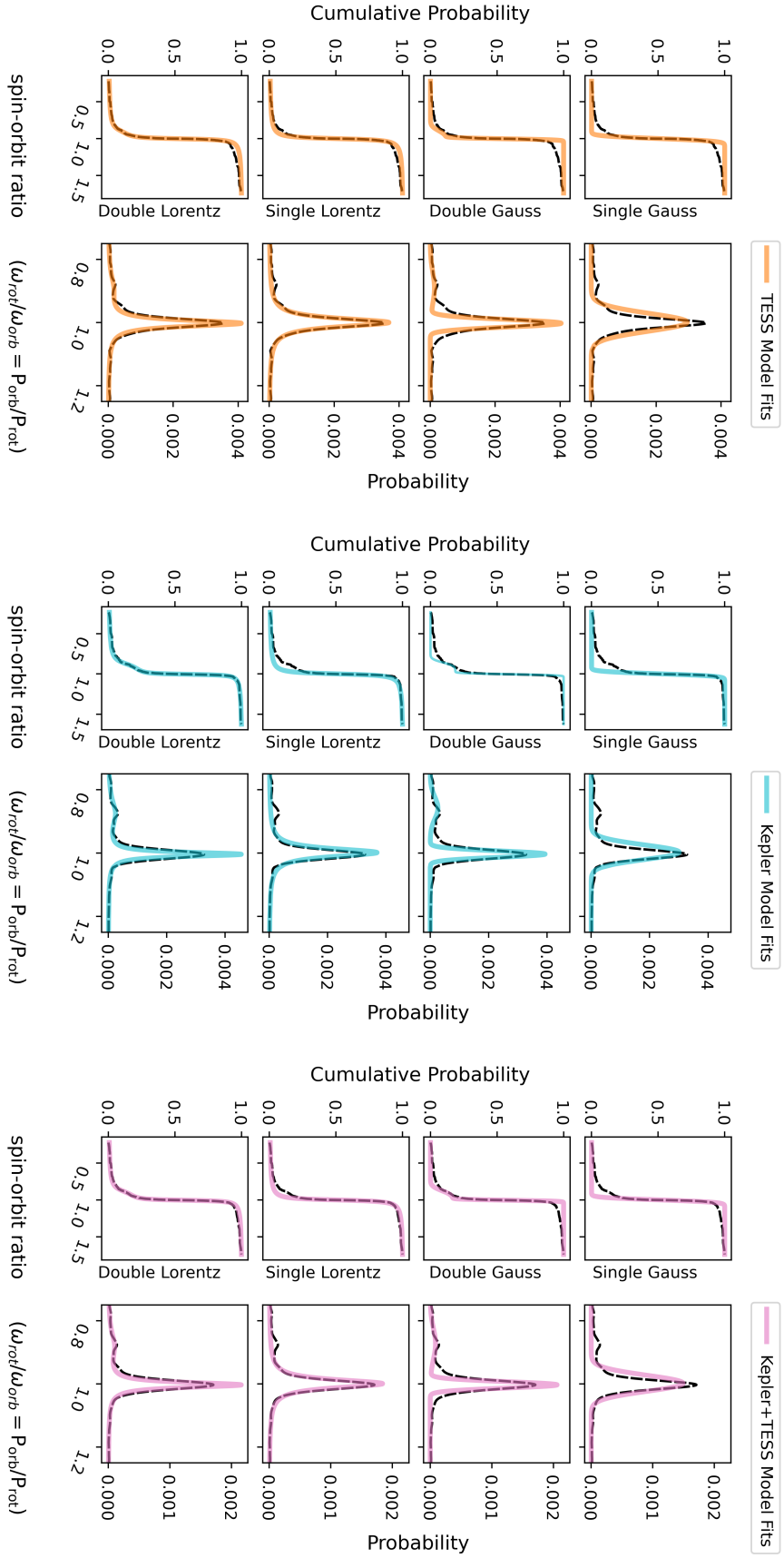


**Figure 18.** Left: Estimation for the cumulative probability density function (CDF) for the combined L17 *Kepler* and *TESS* data sample. The best fit models for the CDF are overlaid for visual comparison. Right: Normalized kernel density estimate of the probability density function (PDF) for the combined L17 *Kepler* and *TESS* data sample. The parameters from the best fit models were used to generate PDF functions that are overlaid for visual comparison.

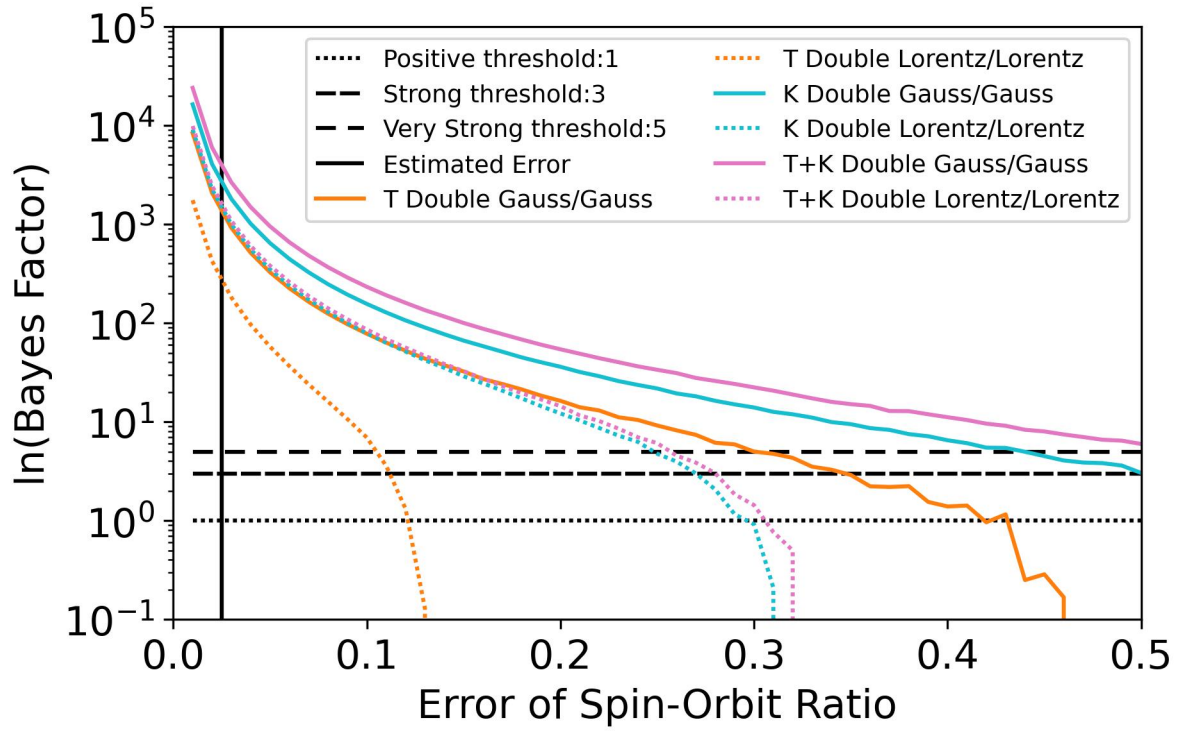


**Figure 19.** Natural log Bayes factors (BF), representing the natural log of the marginal likelihood ratio of two different models, calculated using a variable uniform error value. The  $\ln$  BF favors the numerator of the model ratios. Where T is the *TESS* data, K is the *Kepler* data, and T+K is the combined data set.

	Model	$\mu_1$	$\sigma_1 \gamma_1$	$\mu_2$	$\sigma_2 \gamma_2$	a
T Mean	Single Gauss	0.9990	0.0279	-	-	-
	Double Gauss	1.0023	0.0117	0.8894	0.0489	0.1368
	Single Lorentz	0.9999	0.0159	-	-	-
	Double Lorentz	1.0023	0.0117	0.8894	0.0489	0.1367
T Median	Single Gauss	0.9990	0.0279	-	-	-
	Double Gauss	1.0023	0.0117	0.8909	0.0493	0.1372
	Single Lorentz	0.9999	0.0159	-	-	-
	Double Lorentz	1.0023	0.0117	0.8909	0.0492	0.1369
K Mean	Single Gauss	0.9974	0.0231	-	-	-
	Double Gauss	1.0033	0.0100	0.8572	0.0346	0.2302
	Single Lorentz	0.9985	0.0151	-	-	-
	Double Lorentz	1.0039	0.0079	0.8739	0.0477	0.3096
K Median	Single Gauss	0.9974	0.0231	-	-	-
	Double Gauss	1.0033	0.0100	0.8574	0.0344	0.2301
	Single Lorentz	0.9985	0.0151	-	-	-
	Double Lorentz	1.0039	0.0079	0.8741	0.0483	0.3092
K+T Mean	Single Gauss	0.9981	0.0254	-	-	-
	Double Gauss	1.0029	0.0100	0.8733	0.0489	0.2052
	Single Lorentz	0.9992	0.0154	-	-	-
	Double Lorentz	1.0031	0.0096	0.8791	0.0493	0.2202
K+T Median	Single Gauss	0.9981	0.0254	-	-	-
	Double Gauss	1.0029	0.0100	0.8732	0.0492	0.2052
	Single Lorentz	0.9992	0.0154	-	-	-
	Double Lorentz	1.0031	0.0096	0.8791	0.0493	0.2201

**Table 5.** Weighted mean and weighted median parameters of each posterior. Where T is the *TESS* data, K is the *Kepler* data, and T+K is the combined data set. The parameters are  $\mu_1$  (primary mean),  $\sigma_1|\gamma_1$  (primary standard deviation|half width half maximum),  $\mu_2$  (secondary mean),  $\sigma_2|\gamma_2$  (secondary standard deviation|half width half maximum), a (secondary amplitude). The primary amplitude is always 1, so it is not a parameter.

	Model	Single Gauss	Double Gauss	Single Lorentz	Double Lorentz
<i>TESS</i>	Single Gauss	-	1330	1062	1330
	Double Gauss	-1330	-	-267	0.24
	Single Lorentz	-1062	267	-	267
	Double Lorentz	-1330	-0.24	-267	-
<i>Kepler</i>	Single Gauss	-	2607	1162	2680
	Double Gauss	-2607	-	-1444	73
	Single Lorentz	-1162	1444	-	1572
	Double Lorentz	-2680	-73	-1572	-
Combined	Single Gauss	-	3838	2272	3844
	Double Gauss	-3838	-	-1566	6.2
	Single Lorentz	-2272	1566	-	1572
	Double Lorentz	-3844	-6.2	-1572	-

**Table 6.** Natural log Bayes factors comparing the evidence between each pair of model out of a set of four different candidate models: single Gaussian, double Gaussian, single Lorentzian, and double Lorentzian. As given in equation 6, the natural log Bayes factor  $\ln \mathcal{B} = \ln(\frac{Z_1}{Z_2}) = \ln Z_1 - \ln Z_2$ , where  $Z_1$  is the model listed in the column, and  $Z_2$  is the model listed in the corresponding row.

## 5. CONCLUSION

In L17 a subsynchronous population of EBs was discovered, a phenomenon not previously observed. To determine if this population is an instrumental artifact, we conducted a follow-up study by analyzing 1404 unique TIC IDs in the *TESS* Eclipsing Binary Catalog (TEBC), with *TESS*'s 85% sky coverage.

To ascertain if an EB is subsynchronous, we measured the rotational period through starspot modulation in the light curve. Using a combination of machine learning random forest classifier and visual analysis, we filtered our sample to only include EBs with strong evidence of starspot modulation. Furthermore, we limited our sample to targets with orbital periods  $P_{\text{orb}} < 10$  days, focusing on systems with strong tidal interactions. This resulted in 584 TIC IDs identified as exhibiting strong starspot modulation in their light curves. We determined the rotational period using Lomb-Scargle periodograms, the autocorrelation function, and phase dispersion minimization, recording the best-fit value after visual inspection.

When examining the spin-orbit ratio versus orbital period, there was a subsynchronous weak secondary peak in the *TESS* data. Although not as strong an indicator as the *Kepler* data, this confirms that the subsynchronous EB population observed in L17 is not an artifact specific to the *Kepler* instrument or survey.

To determine statistical significance, we modeled the combined *TESS* and *Kepler* samples alongside the individual datasets. Using Bayesian sampling, we converted the sample into an estimated cumulative distribution function (CDF) and found the best fit parameters. The natural log Bayes factors indicate that a double-peaked distribution is the best fit across data sets, suggesting that the subsynchronous population is statistically significant.

To further investigate whether the by-eye error in rotation period skewed the results, we recalculated the natural log Bayes factors across posteriors with uniform errors ranging from 0.01 to 0.5. Even at large error values, the double-peaked distribution remained a better fit than a single-peaked distribution, affirming the consistency between our measurements and L17.

Despite aligning with the L17 findings, more work is needed to confirm the reality of the population. Our current methods do not measure errors on the rotational periods, leading us to use a uniform value for modeling. Future work could use methods such as Gaussian processes (*e.g.* Angus et al. 2018, 2020; Gordon et al. 2021) to sample posteriors for the rotation period and derive errors for each individual lightcurve.

Understanding this sub-population is crucial, as the majority of stars are in binary systems. Our results indicate that this subpopulation is statistically significant, which has yet to be explained by tidal theory. This dataset provides a starting point for unraveling the mystery of the origins of the subpopulation and better understanding EB evolution.

This paper includes data collected with the *TESS* mission, obtained from the MAST data archive at the Space Telescope Science Institute (STScI). Funding for the *TESS* mission is provided by the NASA Explorer Program. STScI is operated by the Association of Universities for Research in Astronomy, Inc., under NASA contract NAS 5-26555.

This paper includes data collected by the *Kepler* mission and obtained from the MAST data archive at the Space Telescope Science Institute (STScI). Funding for the *Kepler* mission is provided by the NASA Science Mission Directorate. STScI is operated by the Association of Universities for Research in Astronomy, Inc., under NASA contract NAS 5-26555.

This work has made use of data from the European Space Agency (ESA) mission *Gaia* (<https://www.cosmos.esa.int/gaia>), processed by the *Gaia* Data Processing and Analysis Consortium (DPAC, <https://www.cosmos.esa.int/web/gaia/dpac/consortium>). Funding for the DPAC has been provided by national institutions, in particular the institutions participating in the *Gaia* Multilateral Agreement.

*Software:* `astropy` (Astropy Collaboration et al. 2013, 2018), `cesium` (Naul et al. 2016), `dynesty` (Speagle 2020), `exoplanet` (Foreman-Mackey et al. 2021), `lightkurve` (Lightkurve Collaboration et al. 2018)

## APPENDIX

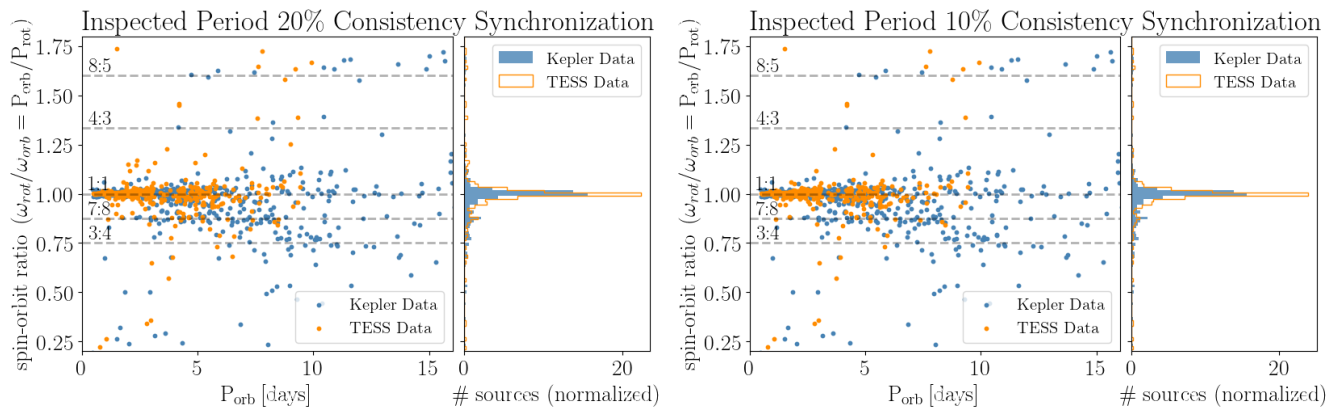


**Figure 20.** Left panel: *TESS* subsample of values with 20% cross-method confidence of the inspected period, plotted alongside the L17 *Kepler* data. Right panel: Same as left figure, but with 10% cross-method confidence.

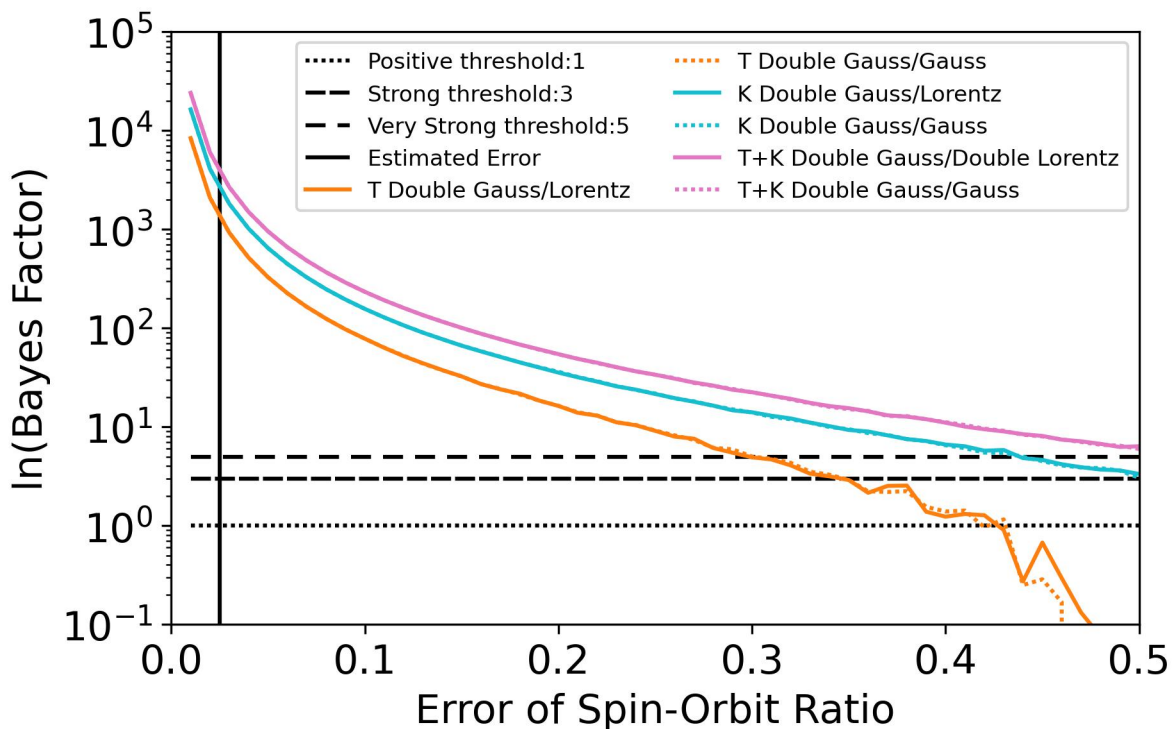


**Figure 21.** Natural log Bayes factors (BF), representing the marginal likelihood ratio of two different models, calculated using a variable uniform error value. The ln BF favors the numerator of the model ratios. Where T is the *TESS* data, K is the *Kepler* data, and T+K is the combined data set. This plot shows that the double Gaussian model is decisively the best fit across all data sets, even at large errors.

## REFERENCES

- Aigrain, S., Pont, F., & Zucker, S. 2012, *Monthly Notices of the Royal Astronomical Society*, 419, 3147, doi: [10.1111/j.1365-2966.2011.19960.x](https://doi.org/10.1111/j.1365-2966.2011.19960.x)
- Anderson, T. W. 1962, *The Annals of Mathematical Statistics*, 33, 1148. <http://www.jstor.org/stable/2237885>
- Angus, R., Morton, T., Aigrain, S., Foreman-Mackey, D., & Rajpaul, V. 2018, *Monthly Notices of the Royal Astronomical Society*, 474, 2094, doi: [10.1093/mnras/stx2109](https://doi.org/10.1093/mnras/stx2109)
- Angus, R., Beane, A., Price-Whelan, A. M., et al. 2020, arXiv:2005.09387 [astro-ph]. <http://arxiv.org/abs/2005.09387>
- Astropy Collaboration, Robitaille, T. P., Tollerud, E. J., et al. 2013, *\aap*, 558, A33, doi: [10.1051/0004-6361/201322068](https://doi.org/10.1051/0004-6361/201322068)
- Astropy Collaboration, Price-Whelan, A. M., Sipőcz, B. M., et al. 2018, *\aj*, 156, 123, doi: [10.3847/1538-3881/aabc4f](https://doi.org/10.3847/1538-3881/aabc4f)
- Bolmont, E., & Mathis, S. 2016, *Celestial Mechanics and Dynamical Astronomy*, 126, 275, doi: [10.1007/s10569-016-9690-3](https://doi.org/10.1007/s10569-016-9690-3)
- Borucki, W. J., Koch, D., Basri, G., et al. 2010, *Science*, 327, 977, doi: [10.1126/science.1185402](https://doi.org/10.1126/science.1185402)
- Carroll, J. A., & Ingram, L. J. 1933, *Monthly Notices of the Royal Astronomical Society*, 93, 508, doi: [10.1093/mnras/93.7.508](https://doi.org/10.1093/mnras/93.7.508)
- Chen, X., Wang, S., Deng, L., et al. 2020, arXiv:2005.08662 [astro-ph]. <http://arxiv.org/abs/2005.08662>
- Claret, A., & Cunha, N. C. S. 1997, *A&A*, 318, 187
- Claytor, Z. R., van Saders, J. L., Llama, J., et al. 2022, *The Astrophysical Journal*, 927, 219, doi: [10.3847/1538-4357/ac498f](https://doi.org/10.3847/1538-4357/ac498f)
- Collaboration, G., Vallenari, A., Brown, A. G. A., et al. 2022, *Gaia Data Release 3: Summary of the content and survey properties*, doi: [10.1051/0004-6361/202243940](https://doi.org/10.1051/0004-6361/202243940)
- Counselman, III, C. C. 1973, *The Astrophysical Journal*, 180, 307, doi: [10.1086/151964](https://doi.org/10.1086/151964)
- David, T. J., Hillenbrand, L. A., Cody, A. M., Carpenter, J. M., & Howard, A. W. 2015, *The Astrophysical Journal*, 816, 21, doi: [10.3847/0004-637X/816/1/21](https://doi.org/10.3847/0004-637X/816/1/21)
- David, T. J., Conroy, K. E., Hillenbrand, L. A., et al. 2016, *The Astronomical Journal*, 151, 112, doi: [10.3847/0004-6256/151/5/112](https://doi.org/10.3847/0004-6256/151/5/112)
- Duchêne, G., & Kraus, A. 2013, *\araa*, 51, 269, doi: [10.1146/annurev-astro-081710-102602](https://doi.org/10.1146/annurev-astro-081710-102602)
- Duquennoy, A., & Mayor, M. 1991, *\aap*, 248, 485
- Fausnaugh, M., Morgan, E., Vanderspek, R., et al. 2021, *PASP*, 133, 095002, doi: [10.1088/1538-3873/ac1d3f](https://doi.org/10.1088/1538-3873/ac1d3f)
- Ferraz-Mello, S., Rodríguez, A., & Hussmann, H. 2008, *Celestial Mechanics and Dynamical Astronomy*, 101, 171, doi: [10.1007/s10569-008-9133-x](https://doi.org/10.1007/s10569-008-9133-x)
- Fleming, D. P., Barnes, R., Davenport, J. R. A., & Luger, R. 2019, *The Astrophysical Journal*, 881, 88, doi: [10.3847/1538-4357/ab2ed2](https://doi.org/10.3847/1538-4357/ab2ed2)
- Foreman-Mackey, D., Luger, R., Agol, E., et al. 2021, *The Journal of Open Source Software*, 6, 3285, doi: [10.21105/joss.03285](https://doi.org/10.21105/joss.03285)
- Gaia Collaboration, Vallenari, A., Brown, A. G. A., et al. 2023, *A&A*, 674, A1, doi: [10.1051/0004-6361/202243940](https://doi.org/10.1051/0004-6361/202243940)
- Gillen, E., Hillenbrand, L. A., David, T. J., et al. 2017, *The Astrophysical Journal*, 849, 11, doi: [10.3847/1538-4357/aa84b3](https://doi.org/10.3847/1538-4357/aa84b3)
- Giuricin, G., Mardirossian, F., & Mezzetti, M. 1984, *A&A*, 141, 227
- Gordon, T. A., Davenport, J. R. A., Angus, R., et al. 2021, *The Astrophysical Journal*, 913, 70, doi: [10.3847/1538-4357/abf63e](https://doi.org/10.3847/1538-4357/abf63e)
- Gray, D. F. 1976, *The observation and analysis of stellar photospheres*. <https://ui.adsabs.harvard.edu/abs/1976oasp.book....G>
- Gustafsson, B., Edvardsson, B., Eriksson, K., et al. 2008, *\aap*, 486, 951, doi: [10.1051/0004-6361:200809724](https://doi.org/10.1051/0004-6361:200809724)
- Howell, S. B., Sobek, C., Haas, M., et al. 2014, *Publications of the Astronomical Society of the Pacific*, 126, 398, doi: [10.1086/676406](https://doi.org/10.1086/676406)
- Hut, P. 1980, *Astronomy and Astrophysics*, 92, 167. <https://ui.adsabs.harvard.edu/abs/1980A&A....92..167H/abstract>
- . 1981, *Astronomy and Astrophysics*, 99, 126. <http://adsabs.harvard.edu/abs/1981A%26A....99..126H>
- Jayasinghe, T., Kochanek, C. S., Stanek, K. Z., et al. 2018, *Monthly Notices of the Royal Astronomical Society*, 477, 3145, doi: [10.1093/mnras/sty838](https://doi.org/10.1093/mnras/sty838)
- Kass, R. E., & Raftery, A. E. 1995, *Journal of the American Statistical Association*, 90, 773, doi: [10.1080/01621459.1995.10476572](https://doi.org/10.1080/01621459.1995.10476572)
- Kim, D.-W., & Bailer-Jones, C. A. L. 2016, *Astronomy & Astrophysics*, 587, A18, doi: [10.1051/0004-6361/201527188](https://doi.org/10.1051/0004-6361/201527188)
- Kirk, B., Conroy, K., Prša, A., et al. 2016, *The Astronomical Journal*, 151, 68, doi: [10.3847/0004-6256/151/3/68](https://doi.org/10.3847/0004-6256/151/3/68)
- Leconte, J., Chabrier, G., Baraffe, I., & Levrard, B. 2010, *Astronomy and Astrophysics*, 516, A64, doi: [10.1051/0004-6361/201014337](https://doi.org/10.1051/0004-6361/201014337)

- Lightkurve Collaboration, Cardoso, J. V. d. M., Hedges, C., et al. 2018, Lightkurve: Kepler and TESS time series analysis in Python, *Astrophysics Source Code Library*. <http://ascl.net/1812.013>
- Lomb, N. R. 1976, *Astrophysics and Space Science*, 39, 447, doi: [10.1007/BF00648343](https://doi.org/10.1007/BF00648343)
- Lurie, J. C., Vyhmeister, K., Hawley, S. L., et al. 2017, *The Astronomical Journal*, 154, 250, doi: [10.3847/1538-3881/aa974d](https://doi.org/10.3847/1538-3881/aa974d)
- Marilli, E., Frasca, A., Covino, E., et al. 2007, *\aap*, 463, 1081, doi: [10.1051/0004-6361:20066458](https://doi.org/10.1051/0004-6361:20066458)
- Matijević, G., Prša, A., Orosz, J. A., et al. 2012, *The Astronomical Journal*, 143, 123, doi: [10.1088/0004-6256/143/5/123](https://doi.org/10.1088/0004-6256/143/5/123)
- Matson, R. A., Gies, D. R., Guo, Z., & Orosz, J. A. 2016, *The Astronomical Journal*, 151, 139, doi: [10.3847/0004-6256/151/6/139](https://doi.org/10.3847/0004-6256/151/6/139)
- Matt, S. P., Brun, A. S., Baraffe, I., Bouvier, J., & Chabrier, G. 2015, *The Astrophysical Journal Letters*, 799, L23, doi: [10.1088/2041-8205/799/2/L23](https://doi.org/10.1088/2041-8205/799/2/L23)
- McQuillan, A., Aigrain, S., & Mazeh, T. 2013, *\mnras*, 432, 1203, doi: [10.1093/mnras/stt536](https://doi.org/10.1093/mnras/stt536)
- McQuillan, A., Mazeh, T., & Aigrain, S. 2014, *\apjs*, 211, 24, doi: [10.1088/0067-0049/211/2/24](https://doi.org/10.1088/0067-0049/211/2/24)
- Meibom, S., & Mathieu, R. D. 2005, *The Astrophysical Journal*, 620, 970, doi: [10.1086/427082](https://doi.org/10.1086/427082)
- Meibom, S., Mathieu, R. D., & Stassun, K. G. 2006, *\apj*, 653, 621, doi: [10.1086/508252](https://doi.org/10.1086/508252)
- Mowlavi, N., Lecoer-Taïbi, I., Holl, B., et al. 2017, *Astronomy & Astrophysics*, 606, A92, doi: [10.1051/0004-6361/201730613](https://doi.org/10.1051/0004-6361/201730613)
- Naul, B., van der Walt, S., Crellin-Quick, A., Bloom, J. S., & Pérez, F. 2016, *CoRR*, abs/1609.04504
- Penev, K., Zhang, M., & Jackson, B. 2014, *Publications of the Astronomical Society of the Pacific*, 126, 553, doi: [10.1086/677042](https://doi.org/10.1086/677042)
- Prsa, A., Kochoska, A., Conroy, K. E., et al. 2021, arXiv:2110.13382 [astro-ph]. <http://arxiv.org/abs/2110.13382>
- Prša, A., Batalha, N., Slawson, R. W., et al. 2011, *The Astronomical Journal*, 141, 83, doi: [10.1088/0004-6256/141/3/83](https://doi.org/10.1088/0004-6256/141/3/83)
- Raghavan, D., McAlister, H. A., Henry, T. J., et al. 2010, *The Astrophysical Journal Supplement Series*, 190, 1, doi: [10.1088/0067-0049/190/1/1](https://doi.org/10.1088/0067-0049/190/1/1)
- Repetto, S., & Nelemans, G. 2014, *Monthly Notices of the Royal Astronomical Society*, 444, 542, doi: [10.1093/mnras/stu1454](https://doi.org/10.1093/mnras/stu1454)
- Richards, J. W., Starr, D. L., Butler, N. R., et al. 2011, *The Astrophysical Journal*, 733, 10, doi: [10.1088/0004-637X/733/1/10](https://doi.org/10.1088/0004-637X/733/1/10)
- Ricker, G. R., Winn, J. N., Vanderspek, R., et al. 2014, in *\procspie*, Vol. 9143, *Space Telescopes and Instrumentation 2014: Optical, Infrared, and Millimeter Wave*, 914320, doi: [10.1117/12.2063489](https://doi.org/10.1117/12.2063489)
- Ricker, G. R., Winn, J. N., Vanderspek, R., et al. 2014, in *Society of Photo-Optical Instrumentation Engineers (SPIE) Conference Series*, Vol. 9143, *Space Telescopes and Instrumentation 2014: Optical, Infrared, and Millimeter Wave*, ed. J. Oschmann, Jacobus M., M. Clampin, G. G. Fazio, & H. A. MacEwen, 914320, doi: [10.1117/12.2063489](https://doi.org/10.1117/12.2063489)
- Shumway, S. 2010, *Time Series Analysis and Its Applications: With R Examples* (Springer International Publishing)
- Skumanich, A. 1972, *\apj*, 171, 565, doi: [10.1086/151310](https://doi.org/10.1086/151310)
- Song, H. F., Meynet, G., Maeder, A., et al. 2018, *Astronomy & Astrophysics*, 609, A3, doi: [10.1051/0004-6361/201731073](https://doi.org/10.1051/0004-6361/201731073)
- Speagle, J. S. 2020, *MNRAS*, 493, 3132, doi: [10.1093/mnras/staa278](https://doi.org/10.1093/mnras/staa278)
- Stassun, K. G., Oelkers, R. J., Pepper, J., et al. 2018, *AJ*, 156, 102, doi: [10.3847/1538-3881/aad050](https://doi.org/10.3847/1538-3881/aad050)
- Stellingwerf, R. F. 1978, *The Astrophysical Journal*, 224, 953, doi: [10.1086/156444](https://doi.org/10.1086/156444)
- Taylor, M. B. 2005, in *Astronomical Society of the Pacific Conference Series*, Vol. 347, *Astronomical Data Analysis Software and Systems XIV*, ed. P. Shopbell, M. Britton, & R. Ebert, 29
- Torres, G., Curtis, J. L., Vanderburg, A., Kraus, A. L., & Rizzuto, A. 2018, *\apj*, 866, 67, doi: [10.3847/1538-4357/aadca8](https://doi.org/10.3847/1538-4357/aadca8)
- Vanderburg, A. 2014, arXiv e-prints, arXiv:1412.1827, doi: [10.48550/arXiv.1412.1827](https://doi.org/10.48550/arXiv.1412.1827)
- Weise, P., Launhardt, R., Setiawan, J., & Henning, T. 2010, *Astronomy and Astrophysics*, 517, A88, doi: [10.1051/0004-6361/201014453](https://doi.org/10.1051/0004-6361/201014453)
- Welsh, W. F. 1999, *PASP*, 111, 1347, doi: [10.1086/316457](https://doi.org/10.1086/316457)
- Witte, M. G., & Savonije, G. J. 2002, *Astronomy & Astrophysics*, 386, 222, doi: [10.1051/0004-6361:20020155](https://doi.org/10.1051/0004-6361:20020155)
- Yates, L., Aandahl, Z., Richards, S. A., & Brook, B. W. 2022, *Cross validation for model selection: a primer with examples from ecology*, arXiv. <http://arxiv.org/abs/2203.04552>
- Yu, C., Li, K., Zhang, Y., et al. 2021, *WIREs Data Mining and Knowledge Discovery*, 11, e1425, doi: [10.1002/widm.1425](https://doi.org/10.1002/widm.1425)

Zanazzi, J. J., & Wu, Y. 2021, *The Astronomical Journal*,  
161, 263, doi: [10.3847/1538-3881/abf097](https://doi.org/10.3847/1538-3881/abf097)